Accepted Manuscript

Thermal effects on high-frequency magnetic-field-induced martensite reorientation in ferromagnetic shape memory alloys: An experimental and theoretical investigation

Shaobin Zhang, Xue Chen, Ziad Moumni, Yongjun He

PII: S0749-6419(18)30101-3

DOI: 10.1016/j.ijplas.2018.04.008

Reference: INTPLA 2336

To appear in: *International Journal of Plasticity*

Received Date: 19 February 2018

Revised Date: 9 April 2018

Accepted Date: 9 April 2018

Please cite this article as: Zhang, S., Chen, X., Moumni, Z., He, Y., Thermal effects on high-frequency magnetic-field-induced martensite reorientation in ferromagnetic shape memory alloys: An experimental and theoretical investigation, *International Journal of Plasticity* (2018), doi: 10.1016/j.ijplas.2018.04.008.

Thermal effects on high-frequency magnetic-field-induced martensite reorientation in ferromagnetic shape memory alloys: An experimental and theoretical investigation

Shaobin Zhang[a], Xue Chen[b], Ziad Moumni[a,c], Yongjun He[a,*]

[a] *IMSIA, UMR 8193 CNRS-EDF-CEA-ENSTA, Université Paris-Saclay*
828 Boulevard des Maréchaux, 91762 Palaiseau Cedex, France
[b] *Faculty of Engineering and Environment, Northumbria University*
Newcastle upon Tyne NE1 8ST, UK
[c] *State IJR Center of Aerospace Design and Additive Manufacturing*
Northwestern Polytechnical University, Xian, Shaanxi 710072, China

Abstract

Ferromagnetic Shape Memory Alloys (FSMAs) exhibit large strains by the magnetic-field-induced martensite reorientation. But, due to the high-frequency field-induced cyclic frictional martensite twin boundary motion in FSMAs, the dissipation heat can cause a large temperature rise. Thus, the output strain amplitude of FSMAs would decrease significantly if the temperature increases to be high enough to trigger the Martensite-Austenite phase transformation. Such thermal effects on the dynamic responses of FSMAs are unclear in literature because most existing dynamic experiments were performed only for a short-time period (a few seconds) to avoid the temperature rise. In this paper, systematic long-time experiments (> 100 seconds) on a Ni-Mn-Ga single crystal are conducted at various levels of magnetic field frequency, initial compressive stress and ambient airflow velocity. It is found that, during the long-time actuation, the specimen temperature increases and then saturates at a certain level (stable temperature) while the strain oscillation evolves to a stable cycle; both the stable temperature and the stable strain amplitude depend on the frequency, the stress level and the heat exchange

*Corresponding author. Tel.: (+33) 169319730; fax: (+33) 169319997. E-mail address:

yongjun.he@ensta-paristech.fr (Yongjun HE)

condition (i.e., ambient airflow velocity). Particularly, when the specimen temperature reaches a critical level to partially transform the martensite to the austenite, the output strain amplitude reduces suddenly because of less martensite reorientation. Changing the ambient heat-exchange condition (by the airflow) can modify the specimen temperature evolution to avoid the phase transformation, but it also changes the behaviors of the martensite reorientation that is sensitive to temperature. Eventually, the output strain amplitude depends on the airflow velocity non-monotonically, i.e., there exists a critical heat exchange condition to achieve the maximum stable strain amplitude. Based on the systematic experiments and a simplified one-dimensional heat-transfer model, the critical condition can be determined. The new experimental phenomena of the thermal effects can be well understood and described by the heat-transfer model. Further, instead of avoiding the temperature rise and the phase transformation, we propose to take advantage of the interaction between the temperature-induced phase transformation and the magnetic-field-induced martensite reorientation to develop a special “isothermal” FSMA actuator with a tunable output strain amplitude and a constant working temperature. This paper provides systematic experimental data and theoretical analysis for understanding the thermo-magneto-mechanical coupling in FSMAs and developing reliable high-frequency long-time running FSMA-actuators.

Keywords: Ferromagnetic shape memory alloys, Long-time high-frequency magnetic actuation, Thermal effects, Phase transformation, Martensite reorientation.

Nomenclature

Symbol	Physical meaning	Unit (or value)
t	Time	s
t_h	Characteristic heat-relaxation time	s
t_h^*	Optimal heat-relaxation time	s
λ	Specific heat capacity per unit volume	4×10^6 $J \cdot m^{-3} \cdot K^{-1}$
B	Magnetic flux density	T
$\Delta\varepsilon$	Output strain amplitude	
$\Delta\sigma$	Stress amplitude	MPa
T_0	Ambient temperature	°C
T_{stable}	Specimen temperature at stable state	°C
R	Radius of a simplified bar	m
q	Heat generation rate	$J \cdot m^{-3} \cdot s^{-1}$
q_{TB}	Heat generation rate from twin-boundary motion	$J \cdot m^{-3} \cdot s^{-1}$
q_{eddy}	Heat generation rate from eddy current	$J \cdot m^{-3} \cdot s^{-1}$
q_{stable}	Total heat generation rate at stable state	$J \cdot m^{-3} \cdot s^{-1}$
$\Delta\varepsilon_{stable}$	Strain amplitude at stable state	
M_s	Martensite start temperature	36.5 °C
M_f	Martensite finish temperature	35.5 °C
A_s	Austenite start temperature	41.5 °C
A_f	Austenite finish temperature	42.2 °C
σ_{tw}	Twinning stress	MPa
σ_{tw}^{I}	Twinning stress of Type I twin boundary	MPa
σ_{tw}^{II}	Twinning stress of Type II twin boundary	MPa
σ_{tw}^{eff}	Effective twinning stress	MPa
ν	Contribution fraction of type I twin boundary in effective twinning stress	
$\Delta\varepsilon^{\text{complete MR}}$	Strain amplitude of complete martensite reorientation	
f_{mag}	Magnetic-field frequency	Hz
f_{strain}	Strain frequency	Hz
σ_{ini}	Initial compressive stress	MPa
V_{air}	Ambient airflow velocity	$m \cdot s^{-1}$

1. Introduction

Ferromagnetic Shape Memory Alloy (FSMA) is a typical smart material with thermo-magneto-mechanical coupling, which can provide a large recoverable deformation (up to 10% strain) by the temperature-, stress- or magnetic-field-induced phase transformation (PT) (Arndt et al., 2006; Bruno et al., 2016; Cisse et al., 2016; Haldar et al., 2014; Kainuma et al., 2006; Karaca et al., 2006; Liu et al., 2014; Rogovoy and Stolbova, 2016; Sehitoglu et al., 2012; Sutou et al., 2004) and the magneto-mechanically-driven martensite reorientation (MR) (Chen et al., 2014, 2013; Cisse et al., 2016; Dai et al., 2018; He et al., 2012, 2011; Heczko et al., 2016; Karaca et al., 2006; Kiefer and Lagoudas, 2005, 2004; Molnar et al., 2008; Murray et al., 2000; O'Handley et al., 2000), leading to various potential engineering applications. Normally, the martensitic phase transformation of FSMA needs to be triggered by a high-level stress or a strong magnetic field, and is accompanied by large latent heat release/absorption that can be used as energy harvesters (Basaran, 2009; Saren et al., 2015; Sayyaadi et al., n.d.) and magneto-caloric refrigerators (Franco and Conde, 2012; Qu et al., 2017; Zhao et al., 2017). On the other hand, the martensite reorientation can be driven by a low stress (~1 MPa) or a weak magnetic field (< 1 Tesla) and has small hysteresis and energy dissipation, which are suitable for the applications such as actuators (Asua et al., 2014; Majewska et al., 2010; Smith et al., 2014; Techapiesancharoenkij et al., 2009; Yin et al., 2016) and sensors (Hobza et al., 2018; Sarawate and Dapino, 2006; Stephan et al., 2011; Yin et al., 2016). Particularly, there exists a special twin boundary (so-called Type II twin boundary) with ultra-low frictional twinning stress (~ 0.2 MPa) during the field- and/or stress-driven martensite reorientation in FSMA Ni-Mn-Ga single crystal, due to the monoclinic distortion of its 10M tetragonal martensite phase (although the deviation is small, e.g., the characteristic angle $\gamma = 90.37°$ is close to 90^o of a tetragonal lattice) (Chulist et al., 2013; Heczko et al., 2013; Liu and Xie, 2003; Pascan et al., 2015; Sozinov et al., 2011; Straka et al., 2012, 2011b; Zou et al., 2017; Zreihan et al., 2016). Such low driving force and small

dissipation make FSMA a promising candidate for actuators.

Although the temperature rise due to the low energy dissipation of martensite reorientation in FSMA is negligible in the slow or quasi-static loading conditions, it cannot be ignored in high-frequency magnetic loadings (> 100 Hz) because the dissipation due to the frictional twin boundary motion of martensite reorientation (Blanter et al., 2007; Cui et al., 2017; He et al., 2012, 2011; Heczko et al., 2016; Karaca et al., 2006; Kiefer and Lagoudas, 2005, 2004; Molnar et al., 2008; Murray et al., 2000; O'Handley et al., 2000; Pagounis et al., 2014; Yu et al., 2015) and the eddy current inside the material can accumulate quickly to induce significant temperature rise (Henry, 2002; Henry et al., 2002; Lai, 2009; Lai et al., 2008). Moreover, several physical properties related to martensite reorientation of FSMA are sensitive to the temperature (Aaltio et al., 2008; Adachi et al., 2017; Glavatska et al., 2002; Heczko et al., 2018; Heczko and Straka, 2003; Okamoto et al., 2008; Soroka et al., 2018; Sozinov et al., 2017; Straka et al., 2011a, 2006, 2016, 2012; Vronka et al., 2017; Zreihan et al., 2016). That is why most existing high-frequency dynamic experiments on FSMA were performed only for a short-time period to avoid significant temperature rise (Henry, 2002; Henry et al., 2002; Lai, 2009; Lai et al., 2008). In such short-time experiments, although the output strain seems to be stable with nearly constant strain amplitude, the temperature of the specimen keeps increasing without reaching the steady state, e.g., the temperature increasing rate during the short-time actuation of 20 seconds is larger than 0.5 °C /s in (Pascan et al., 2015) and 0.3 °C/s in (Lai, 2009). Therefore, such short-time actuation systems are not strictly stable since not all the thermo-magneto-mechanical responses have reached the steady states. Thus, it's still unknown whether the large output strain of FSMA under high-frequency magnetic loadings reported in the literature can be guaranteed for the long-time performance (e.g., > 100 s) or not.

One of the main problems caused by the temperature rise is the temperature-induced Martensite-to-Austenite (M-to-A) phase transformation (Auricchio

et al., 2014; Bhattacharya, 2003; Iadicola and Shaw, 2004; Otsuka and C. M. Wayman, 1998), which will disturb the field-induced martensite reorientation in the long-time actuation of FSMA. To the authors' best knowledge, studies about the effect of phase transformation on the martensite reorientation of FSMA are seldom reported in the literature. This is possibly due to the fact that the stress and magnetic field levels for martensite reorientation are too small to trigger the phase transformation (Haldar et al., 2014; Karaca et al., 2006, 2009), and that the energy dissipation of martensite reorientation per cycle is small (Chen et al., 2013; Karaca et al., 2006). However, in the high-frequency magnetic loadings (e.g., beyond 100 Hz, such high-frequency working condition is a main advantage of FSMA actuators over the traditional shape memory alloy (SMA) actuators), the small dissipation heat can accumulate and thus generate significant temperature rise (Lai, 2009; Pascan, 2015; Pascan et al., 2015) especially when the ambient heat exchange is weak (e.g., in still air). The effects of ambient heat exchange on the phase transformation and the mechanical deformation of traditional SMAs have been reported in the literature such as (Blanter et al., 2007; Brinson et al., 2004; He et al., 2010; He and Sun, 2011, 2010; Shaw and Kyriakides, 1995). It is predicted that controlling the ambient heat exchange condition can be a solution to the problem of the temperature rise in FSMA under high-frequency magnetic loadings. Therefore, in our current studies on the long-time high-frequency magnetic actuation of FSMA, ambient airflow of various velocities is forced to pass through the FSMA specimen so that the specimen can be in different heat exchange conditions. Different stable states were finally reached in the specimen, and we found a **non-monotonic** dependence of the output strain amplitude on the airflow velocity. Based on such dependence and a heat balance analysis, the thermal effects on the dynamic behaviors of FSMA are revealed for the first time. Further, the critical thermo-magneto-mechanical conditions to achieve a large stable output strain are provided.

It is normally expected that, when the ambient airflow (heat exchange efficiency) is sufficiently **strong** (of large velocity), the specimen temperature can be kept lower

than the phase transformation temperature (such as the Austenite starting temperature A_s or the Martensite finishing temperature M_f) so as to avoid the phase transformation and maintain the large strain amplitude of the field-induced martensite reorientation. However, in our current studies we found that while the phase transformation can be avoided, the output strain amplitude of FSMA was reduced significantly when the steady-state temperature was much lower than A_s or M_f. This is attributed to the fact that the internal friction of martensite reorientation is sensitive to temperature: the frictional twinning stress for the Type I twin boundary increases with decreasing temperature (Heczko and Straka, 2003; Soroka et al., 2018; Sozinov et al., 2017; Straka et al., 2012, 2011a, 2006). Therefore, for the optimal condition of the largest stable cyclic strain in dynamic actuation, the temperature of FSMA should be kept close to (but lower than) the characteristic phase transformation temperature by applying a proper ambient airflow.

On the other hand, if the applied airflow is **weak** (of low velocity), the FSMA specimen temperature can reach A_s, triggering M-to-A phase transformation. It was revealed in our current experiments that the phase transformation occurred locally: only part of the specimen underwent M-to-A phase transformation, and the remaining untransformed part (M-phase) still kept the cyclic martensite reorientation under the magnetic actuation. So the output strain depended on the fraction of the remaining martensite. It is a spontaneous self-organization process that the specimen adjusted the fraction of the remaining martensite so as to reach the heat balance between the heat transferred by the airflow and the heat generated from the eddy current and the martensite reorientation of the remaining martensite. It was found in our current studies that the stable output strain (corresponding to the fraction of the remaining M-phase) was sensitive to the ambient heat exchange condition (i.e., airflow velocity), while the stable temperature of the specimen was always around M_f. In other words, we found a special type of long-time FSMA actuator whose working temperature (steady-state temperature) always keeps constant around M_f and whose output strain amplitude can be

controlled by the ambient airflow. The new phenomena revealed in our experiments can be well understood and described by the theoretical analysis based on a heat-transfer model. This experimental and theoretical study is expected to provide fundamental information for understanding and modeling of the thermo-magneto-mechanical coupling in the dynamic actuation of FSMAs.

The remaining of this paper is organized as follows: Section 2 introduces the material properties, experimental setup and the testing programs. Section 3 reports the experimental results of various magnetic field frequencies, stress levels and ambient conditions. The data analysis and a heat-transfer model are presented in Section 4. Finally, the summary and conclusions are provided in Section 5.

2. Experimental setup and testing procedures

2.1 Material properties and experimental setup

A $Ni_{50}Mn_{28}Ga_{22}$ (at. %) single crystal rectangular bar with dimensions in 2×3×15 mm (from ETO Magnetic GmbH) were used in the experiments. The specimen is in the state of 10M martensite phase at room temperature. All faces of the specimen were cut parallel to the {100} planes of the parent cubic austenite (with the derivation of less than 2°). From a DSC (differential scanning calorimetry) test, the material characteristic transformation temperatures M_f, M_s, A_s and A_f were obtained as 35.5 °C, 36.5 °C, 41.5 °C and 42.2 °C, respectively. The specimen was installed into a magneto-mechanical loading system as shown in Fig. 1. A high-frequency magnetic field (with magnetic flux density $\boldsymbol{B}$ cyclically varying between ± 0.78 Tesla in a triangle waveform) is applied horizontally along the *x*-direction while a compressive stress is applied vertically by a spring along the *y*-direction. The deformation of the specimen along *y*-direction is measured by a laser displacement sensor (Keyence LK-H027) at the top of the upper specimen holder, and the specimen temperature is measured by a thermocouple (K-type, 0.5 mm sheath diameter) attached at the bottom surface of the

specimen. A force sensor (Kistler 9301B) under the lower specimen holder measures the compressive stress. In order to reduce the heat conduction from the specimen to the fixtures, the specimen holders at the two ends of the specimen are made of plexiglass with low heat conductivity. Thus, it is assumed that the heat exchange is mostly governed by the heat convection via the specimen surface rather than the heat conduction via the specimen ends. To accurately describe the strain and stress evolutions, the displacement and force sensors are set to acquire 25 data points per cycle. For the temperature measurements, the thermocouple is set at the maximum sampling rate of 170 Hz which helps us capture the global temperature variation versus time. During tests, all the deformation, force and temperature data are acquired synchronously (with time accuracy of 10^{-7} s) by using Labview platforms and data acquisition devices (National Instruments USB 6251). In addition, during the dynamic actuation, a CMOS camera of 2048×1088 pixels (Basler acA2000-340 km) with Nikkor lens is used to record the specimen surface morphology (in a gauge section of around 5 mm). Then the recorded optical images are processed by Digital Image Correlation (DIC) software Vic-2D (Correlated Solutions) to obtain the local strain fields.

2.2 Testing programs

Before each test, the specimen is fully compressed along *y*-direction to reach the single variant state with the short-axis (*c*-axis) along *y*-direction (so-called stress-preferred variant, shown as V1 in Fig. 1(b)), which is the reference state (i.e., zero strain) for the calculation of the specimen deformation strain in this paper. Note that the austenite phase is $L2_1$ cubic with a lattice constant of a_0 and the martensite variants are slightly monoclinic, but here we assume that they are tetragonal with two long axes "*a*" and one short axis "*c*" for the simplicity of the analysis. At the beginning of each test, an initial compressive stress σ_{ini} is applied on the specimen by compressing a spring with the aid of a micrometer screw (see Fig. 1(a)). Then a magnetic field of certain frequency f_{mag} is applied to drive the cyclic martensite reorientation between V1 and V2 (so-called

field preferred variant with the short axis along *x*-direction) as shown in Fig. 1(b). During the martensite reorientation, the specimen length changes, leading to a change in the spring length so that the compressive stress also changes. The interaction between the cyclic magnetic field and the evolving compressive stress eventually leads to the cyclic martensite reorientation between the variants V1 and V2. According to previous literature (Heczko et al., 2002; Murray et al., 2000; Straka et al., 2006), the lattice parameters $a \approx 0.595$ nm and $c \approx 0.561$ nm for 10M martensite and $a_0 \approx 0.584$ nm for cubic austenite at room temperature. So the strain along *y*-direction is around 6% when V1 changes to V2 ($(a\text{-}c)/c \approx 6\%$) and around 4% when V1 transforms to cubic austenite ($(a_0\text{-}c)/c \approx 4\%$). It is noted that the lattice parameters are temperature dependent (Glavatska et al., 2002; Pagounis et al., 2014; Straka et al., 2006), so the strain value is temperature dependent also. However, in the current experiments with the small temperature variation (i.e., from the room temperature (≈ 20 °C) to the martensite start temperature M_s = 36.4 °C), the temperature-induced variations in the martensite reorientation strain and the phase transformation strain can be ignored.

The long-time dynamic tests (duration time $t \geq 100$ s) were first conducted in the normal ambient condition (i.e., still air at room temperature 20 ± 2 °C) to demonstrate the dependence of the output strain on the magnetic-field frequency f_{mag} (50 ~ 200 Hz) and the initial compressive stress σ_{ini} (0.1 MPa ~ 4 MPa). From these tests, the significant difference in the output strain between the short-time actuation ($t \approx 10$ s) and the long-time actuation ($t \geq 100$ s) was shown. Secondly, some magneto-mechanical loadings of proper f_{mag} and σ_{ini} (which have the potential to provide large strains) were chosen, and the tests were performed in different ambient conditions (with airflow velocity V_{air} varying from 0 m/s to 60 m/s and airflow temperature was around 16 °C) to study the dependence of the steady-state output strain and the steady-state temperature on the heat exchange efficiency, which can be characterized by a characteristic heat-relaxation time t_h detailed in Appendix A. The t_h is associated with the airflow velocity: for the airflow velocity V_{air} changing from 60 m/s to 0 m/s, t_h changes

correspondingly from 2.2 s to 68.9 s in the current system.

3. Experimental results

The results of the tests without and with the ambient airflow are reported in the following two subsections emphasizing the long-time actuation influence and the ambient thermal effect on the dynamic magnetic-field-induced deformation respectively.

3.1 Effect of long-time actuation

A typical result of the thermo-mechanical responses of the specimen is demonstrated in Fig. 2, where the applied magnetic field frequency f_{mag} is 90 Hz and the initial compressive stress σ_{ini} is 0.4 MPa. It should be noted that all the tests in this subsection were conducted in the still air (i.e., $V_{air} = 0$). The observations of the measured output strain, stress and temperature are given below:

(1) The strain changed cyclically with the magnetic field, and its frequency was two times the magnetic-field frequency: $f_{strain} = 2 \cdot f_{mag} = 180$ Hz as shown in Fig. 2(b) for the short-time responses at $t \approx 8$ s and Fig. 2(c) for the long-time responses at $t \approx 100$ s. The strain amplitude (the difference between the maximum and the minimum output strains in a cycle) of the short-time actuation (< 10 s) was 5.9%, much larger than that (1.0%) of the long-time actuation (> 100 s). A significant reduction in the strain amplitude (so-called strain drop) occurred at $t = 10 \sim 11$ s. After the strain drop, the output strain amplitude $\Delta\varepsilon$ kept constant until the end of the test: the applied magnetic field was turned off at $t \approx 117$ s, from which the strain gradually decreased to 0.8% since the initial compressive stress of 0.4 MPa was not large enough to completely compress V2 back to V1 in the quasi-static condition.

(2) The stress oscillated at the same frequency as the strain. During the strain drop, the stress amplitude $\Delta\sigma$ (the difference between the maximum and minimum

stresses) reduced from 2.8 MPa to 0.8 MPa. Due to the nonlinearity in the stress-strain relation of the martensite reorientation and the inertial effect in the high-frequency dynamic deformation (Henry, 2002; Lai et al., 2008; Pascan et al., 2016; Techapiesancharoenkij et al., 2011, 2009), the shape of the stress oscillation is different from that of the strain oscillation which is close to sinusoidal wave.

(3) The temperature increased rapidly until the strain drop. Then it slightly decreased and finally reached a stable temperature (i.e., steady–state temperature) T_{stable} of 35.8 ^{o}C which is close to the martensitic phase transformation temperatures of the specimen (i.e., M_f = 35.5 ℃ and M_s= 36.5 ℃).

It is seen from this test that the large temperature increasing rate (around 1.6 ℃/s) and the large output strain amplitude ($\Delta\varepsilon$ = 5.9%) during the short-time actuation (< 10 s) cannot be maintained when the temperature increases to a high level at which strain drop takes place. The temperature and the strain amplitude finally reach a steady state (stable for a long time t > 100s), and the steady-state strain amplitude is much smaller than that of the short-time actuation. Such strain drop in the long-time actuation was observed in many tests of various loading conditions such as the ones with different magnetic field frequencies in Fig. 3 and the ones with different initial stresses in Fig. 4. Table 1 summarizes the output strain amplitude $\Delta\varepsilon$ of all the tests (f_{strain} = 100 Hz ~ 400 Hz and σ_{ini} = 0.2 MPa ~ 4 MPa): the values in the small red font are the unstable $\Delta\varepsilon$ before the strain-drop while the values in the big black font are the stable $\Delta\varepsilon$ after the strain-drop. The cases with only the values in the big black font show no strain-drop in the actuation. It is seen that almost all the large strain amplitudes (> 1%) are not stable. As an example, the stable and unstable values of $\Delta\varepsilon$ at σ_{ini} = 0.4 MPa in Table 1 are plotted in Fig. 5. It is confirmed by this figure that in the steady state, only the small strain amplitude (less than 1.5% for cases shown in Fig. 5) can be obtained from the

current tests conducted in still air (i.e., weak ambient heat exchange). In addition, it's seen from Fig. 5 and Table 1 that, for a given initial stress, the unstable strain amplitude $\Delta\varepsilon_{\text{unstable}}$ depends on the strain frequency non-monotonically (with the maximum strain amplitude at the resonance frequency). This frequency effect in the dynamic actuation of FSMAs has been experimentally observed (Henry, 2002; Lai et al., 2008; Pascan et al., 2016; Techapiesancharoenkij et al., 2011, 2009) and theoretically modelled by considering the inertial effect of the dynamic systems (Faran et al., 2017; Faran and Shilo, 2016; Henry, 2002; Sarawate and Dapino, 2008; Tan and Elahinia, 2008) .

The stable temperature (steady-state temperature) of all the tests are summarized in Fig. 6. It is seen that all the cases with the strain-drop behavior (marked by the red dashed rectangle) have the stable temperatures around the martensitic transformation temperatures (M_s or M_f) while those without the strain-drop behavior have the stable temperatures well below M_f. This implies that the strain-drop is caused by the temperature-induced Martensite-to-Austenite phase transformation. When the temperature at some local positions of the specimen reaches the phase transformation temperature (A_s or A_f), the material transforms from M phase to A phase at these positions. Then these positions contribute little to the nominal cyclic strain. The appearance of A phase during strain-drop can also be confirmed by the local strain field evolution of the specimen based on the in-situ optical observation and the associated DIC strain maps.

The local strain fields at two typical instants (before and after the strain drop) are shown in Figs. 2(d) and (e), which correspond to the nominal strain oscillations in Figs. 2(b) and (c), respectively. It should be noted that all the local strains are calculated with respect to the pre-compressed state (stress-preferred variant V1 with the short axis *c* along *y*-direction). It is seen from Fig. 2(d) that the local strains of all the material points in the gauge section change to around 6% when the nominal strain reaches $\varepsilon_{\max}$ (which means that all the material becomes the field-preferred martensite variant V2),

and around 0% when the nominal strain reaches ε_{min} (all the material returns to the stress-preferred martensite variant V1). The combination of Figs. 2(b) and (d) indicates that a cyclic complete martensite reorientation with the nominal strain 5.9% is achieved in the whole specimen before the strain drop (i.e., all the material points in the specimen are taking cyclic martensite reorientation).

By contrast, the local strain distributions in Fig. 2(e) show that almost all the points in the gauge section have a constant local strain around 4% when the specimen responses reach the stable state (after the strain drop as shown in Fig. 2(c)). This indicates that the applied cyclic magnetic field cannot drive the martensite reorientation in these zones (non-active zone with constant local strain). Based on the fact that the theoretical strain of the Austenite phase with respect to the Martensite variant V1 is 4% in our specimen as calculated in Section 2.2, it's implied that the material points in the non-active zones (with constant local strain 4%) are in the state of A-phase, thus not sensitive to the applied cyclic magnetic field (contributing little to the nominal cyclic strain). Combining the nominal strain oscillation in Fig. 2(c), the local strain distribution in Fig. 2(e) and the steady-state temperature around M_s and M_f in Fig. 6, we can conclude that the strain-drop behavior is caused by the temperature-rise induced Martensite-to-Austenite phase transformation, and A-phase is non-active under the current weak magnetic field.

3.2 Effect of the ambient heat exchange

To avoid the large temperature rise (so as to avoid the strain-drop due to phase transformation), **strong** ambient airflows were forced to pass through the specimen during the long-time actuation tests shown in Figs. 7(a), (b) and (c) (all these tests were conducted at f_{strain} = 180 Hz and σ_{ini} = 0.4 MPa.) where the air velocity V_{air} is 60 m/s, 35 m/s and 15 m/s, respectively (the characteristic heat-relaxation time t_h is 2.2s, 4.2s and 8.8s correspondingly). It is seen that their stable temperatures are 18.3 ^{o}C, 24.5 ^{o}C and 33.8 ^{o}C, well below M_f so that there is no phase transformation (no strain-drop process)

in these tests. It is also noted that the stable strain amplitude $\Delta\varepsilon_{stable}$ increases from 1.5% to 5.4% when the air velocity V_{air} decreases from 60 m/s to 15 m/s (or when the stable temperature T_{stable} increases from 18.3 ^{o}C to 33.8 ^{o}C). The reason for such temperature dependence or the airflow dependence will be discussed in Section 4.

By contrast, when only a **weak** airflow was applied, the temperature rise is still high enough to trigger the strain-drop process (the phase transformation) as shown in Figs. 7(d), (e) and (f) where $\Delta\varepsilon_{stable}$ = 3.6%, 2.5% and 1.0% with the airflow velocity V_{air} = 8 m/s, 3 m/s and 0 m/s (still air), respectively. The corresponding characteristic heat-relaxation time t_h = 14.0 s, 22.2 s and 68.9 s. It is seen that the stable temperatures of the three cases are 34.9 °C, 35.9 °C and 36.1 °C; all are close to M_f and M_s.

Figure 8 summarizes the stable strain amplitude and the stable temperature ($\Delta\varepsilon_{stable}$ and T_{stable}) of the systematic tests at different levels of the ambient airflow velocity V_{air} (also the corresponding characteristic heat-relaxation time t_h). It is seen that $\Delta\varepsilon_{stable}$ changes non-monotonically with t_h (or V_{air}). The maximum strain amplitude can be achieved at t_h^* ≈ 8.8 s for f_{strain} = 180 Hz in Fig. 8(a) and at t_h^* ≈ 11.7 s for f_{strain} = 220 Hz in Fig. 8(b). For both frequencies, the stable temperature T_{stable} increases with increasing t_h (decreasing V_{air}) and the saturated temperature is at around 36 ^{o}C when t_h is large enough (i.e., when the airflow is weak). Two important conclusions can be obtained from Fig. 8:

(1) Optimal condition of heat exchange to achieve the largest stable strain amplitude: For a given magneto-mechanical loading of f_{mag} ($= \frac{f_{strain}}{2}$) and σ_{ini}, a proper ambient condition (e.g. with a proper value of t_h (or V_{air})) setting the stable temperature of the specimen close to (but lower than) M_f without triggering the Martensite-to-Austenite phase transformation can lead to the maximum stable strain amplitude of the specimen, e.g., t_h^* = 8.8 s in Fig. 8(a) and 11.7 s in Fig. 8(b).

(2) A special "isothermal" FSMA actuator with tunable output strain amplitude by ambient heat exchange can be developed: In the range of weak ambient heat exchange (i.e., $t_h > 8.8$s in Fig. 8(a) and $t_h > 11.7$s in Fig. 8(b)), the specimen's stable strain amplitude can be adjusted by controlling t_h (or V_{air}) while keeping its stable temperature constant around M_f, e.g., see the red circle points in Figs. 8(a) and 8(b). The understanding and modeling on these behaviors are discussed in the next section.

4. Theoretical study on the effect of ambient heat exchange

In this section, we discuss first the mechanisms for the non-monotonic dependence of the output stable strain on the ambient air velocity, and then the optimal conditions to achieve a large stable strain.

4.1 Non-monotonic dependence of stable strain amplitude on ambient airflow

Both the $\Delta\varepsilon_{stable}$-$t_h$ curves and the T_{stable}-t_h curves in Fig. 8 can be divided into two regions: the region of strong heat exchange ($t_h < t_h^*$ where there is no strain drop and the stable temperature increases with t_h) and the one of weak heat exchange ($t_h > t_h^*$ where the strain drop takes place and the temperature keeps constant). That means the heat-relaxation time t_h-dependences in these two regions should be governed by different mechanisms, which will be discussed respectively in the following two subsections.

4.1.1 Region of strong ambient heat exchange (without phase transformation)

As the heat exchange has important effects on the temperature rise and the stable strain, a heat-transfer model is adopted to facilitate the following analysis and discussion. The FSMA specimen is modeled as a one-dimension (1D) bar shown in Fig. 9. The temperature evolution of an elementary length dx of the bar during the cyclic martensite reorientation can be calculated by the following heat balance equation

(Bruno et al., 1995; He and Sun, 2011; Pascan et al., 2015):

$$\lambda \cdot \pi R^2 \cdot dx \cdot dT = q \cdot \pi R^2 \cdot dx \cdot dt - 2\pi R \cdot dx \cdot h \cdot (T - T_0) \cdot dt \quad (1)$$

where the parameters T_0, R, λ, q and h denote the ambient temperature, the radius of the bar, the material heat capacity per unit volume, the heat generation rate and the heat convection coefficient, respectively. The temperature of the bar is assumed to be uniform, only depends on time: $T(t)$. Heat conduction is neglected in Eq. (1), and we can further reduce this equation to

$$\frac{dT}{dt} = \frac{q}{\lambda} - \frac{2h}{\lambda \cdot R} \times (T - T_0) \quad (2)$$

There are two contributions to the heat generation rate q ($\mathrm{J \cdot m^{-3} \cdot s^{-1}}$): (1) q_{TB} ($= 2\sigma_{\mathrm{tw}} \cdot \Delta\varepsilon \cdot f_{\mathrm{strain}}$) from the martensite reorientation (with σ_{tw} being the twinning stress) and (2) the energy dissipation from the field-induced eddy current inside the specimen q_{eddy}. The details about the measurement on the eddy-current dissipation can be found in Appendix B, where q_{eddy} has a relation with the strain frequency by data fitting: $q_{\mathrm{eddy}} = 2320.7 \cdot f_{\mathrm{strain}} - 1.35 \times 10^5$ ($\mathrm{J \cdot m^{-3} \cdot s^{-1}}$) for current system with the strain frequency f_{strain} in the range of [100 Hz, 400 Hz]. By introducing $q = q_{\mathrm{TB}} + q_{\mathrm{eddy}}$ into Eq. (2), we obtain:

$$\begin{aligned} \frac{dT}{dt} &= \frac{(q_{\mathrm{TB}} + q_{\mathrm{eddy}})}{\lambda} - \frac{2h}{\lambda \cdot R} \cdot (T - T_0) \\ &= \frac{(q_{\mathrm{TB}} + q_{\mathrm{eddy}})}{\lambda} - \frac{1}{t_h} \cdot (T - T_0) \end{aligned} \quad (3)$$

where $t_{\mathrm{h}} = \frac{R \cdot \lambda}{2h}$ is the characteristic heat-relaxation time, which can be measured by the heat-relaxation experiments as shown in Appendix A.

The solution to Eq. (3) is

$$T = T_0 + \frac{q_{\mathrm{TB}} + q_{\mathrm{eddy}}}{\lambda} \cdot t_{\mathrm{h}} \cdot \left(1 - e^{-\frac{t}{t_{\mathrm{h}}}}\right) \quad (4)$$

Then the temperature rise ΔT can be obtained from Eq. (4) as:

$$\Delta T = T - T_0 = \frac{q_{\mathrm{TB}} + q_{\mathrm{eddy}}}{\lambda} \cdot t_{\mathrm{h}} \cdot \left(1 - e^{-\frac{t}{t_{\mathrm{h}}}}\right) \tag{5}$$

Equation (5) can be used to describe the temperature rise observed in the experiments. Taking the test in Fig. 7(c) as an example, with $\Delta\varepsilon$ = 5.4%, t_{h} = 8.8 s, f_{strain} = 180 Hz, σ_{tw} = 0.35 MPa and $\lambda = 4 \times 10^6$ J·m^{-3}·K^{-1}, we plot Eq. (5) in Fig. 10. It's seen that Eq. (5) agrees well with the experimental data.

The more important capability of this heat-transfer model is to predict the steady-state responses. By taking t to be infinity in Eq. (5), we obtain the stable temperature T_{stable} as:

$$\Delta T_{\mathrm{stable}} = T_{\mathrm{stable}} - T_0 = \frac{t_{\mathrm{h}} \cdot q_{\mathrm{stable}}}{\lambda} \tag{6}$$

where $q_{\mathrm{stable}} = 2\sigma_{\mathrm{tw}} \cdot \Delta\varepsilon_{stable} \cdot f_{\mathrm{strain}} + q_{\mathrm{eddy}}$. It is seen that the stable temperature is related to the stable strain amplitude. In this equation, only twinning stress cannot be directly measured. The twinning stresses of Type I and Type II twin boundaries are different in value in Ni-Mn-Ga single crystal. Moreover, their temperature dependences are also different, e.g., the two shaded zones in Fig. 11 represent the ranges of the experimental measured temperature-dependent twinning stresses in the literature (Heczko and Straka, 2003; Soroka et al., 2018; Sozinov et al., 2017; Straka et al., 2012; Zreihan et al., 2016): the twinning stress of Type II twin boundary is independent of temperature while that of Type I decreases linearly with temperature:

$$\sigma_{\mathrm{tw}}^{\mathrm{I}} = 0.2 - 0.04 \cdot (T - A_{\mathrm{s}}) \quad \text{(MPa)} \tag{7a}$$

$$\sigma_{\mathrm{tw}}^{\mathrm{II}} = 0.2 \quad \text{(MPa)} \tag{7b}$$

In the high-frequency magnetic-field-induced martensite reorientation, both Type I and II twin boundaries can be nucleated (Pascan et al., 2015) and fine twin microstructures can be formed (Chmielus et al., 2008; Yin et al., 2016). Therefore, the effective twinning stress (corresponding to the effective energy dissipation) should

include the contributions from both types of twin boundaries:

$$\begin{aligned}\sigma_{\mathrm{tw}}^{\mathrm{eff}} &= v\cdot\sigma_{\mathrm{tw}}^{\mathrm{I}} + (1-v)\cdot\sigma_{\mathrm{tw}}^{\mathrm{II}} \\ &= v\cdot[0.2-0.04\cdot(T-A_{\mathrm{s}})] + (1-v)\cdot 0.2 \\ &= 0.2-0.04\cdot v\cdot(T-A_{\mathrm{s}})\end{aligned} \tag{8}$$

where v denotes the contribution fraction of type I twin boundary. Substituting Eq. (8) into Eq. (6), we obtain the following relation between the stable temperature and the stable strain amplitude:

$$\begin{aligned}&T_{\mathrm{stable}}-T_0 \\ &=\frac{t_{\mathrm{h}}}{\lambda}\cdot\left\{2\cdot\Delta\varepsilon_{\mathrm{stable}}\cdot f_{\mathrm{strain}}\cdot[0.2-0.04\cdot v\cdot(T_{\mathrm{stable}}-A_{\mathrm{s}})]+q_{\mathrm{eddy}}\right\} \\ &=\frac{t_{\mathrm{h}}}{\lambda}\cdot\{2\cdot\Delta\varepsilon_{\mathrm{stable}}\cdot f_{\mathrm{strain}}\cdot[0.2-0.04\cdot v\cdot(T_{\mathrm{stable}}-A_{\mathrm{s}})] \\ &\qquad +(2320.7\cdot f_{\mathrm{strain}}-1.35\times10^{5})\}\end{aligned} \tag{9a}$$

$$\Rightarrow\Delta\varepsilon_{\mathrm{stable}}=\frac{\left[\frac{(T_{\mathrm{stable}}-T_0)\cdot\lambda}{t_{\mathrm{h}}}-(2320.7\cdot f_{\mathrm{strain}}-1.35\times10^{5})\right]}{2\cdot f_{\mathrm{strain}}\cdot[0.2-0.04\cdot v\cdot(T_{\mathrm{stable}}-A_{\mathrm{s}})]} \tag{9b}$$

In Eq. (9b), only the fraction v cannot be directly measured; but it can be determined by data fitting of the tests without strain drop ($t_h < t_h^*$). Because the specimen temperature T_{stable} also depends on t_h for these tests, we first obtain the relation between T_{stable} and t_h by fitting (see insets in Figs. 12(a) and 12(c) for f_{strain} = 180 Hz and 220 Hz respectively). Then the T_{stable}-t_h relation is substituted into Eq. (9b) to compare with the experimental data and to further determine the parameter v. We find that v = 0.60 and 0.38 respectively for f_{strain} = 180 Hz and 220 Hz can make Eq. (9b) best fit with the experimental data in terms of $\Delta\varepsilon_{stable}$ and (T_{stable}-A_s) in Figs. 12(a) and 12(c). That means the fraction v of Type I twin boundary depends on the loading frequency. It is true for the current system and the previous study (Pascan et al., 2015) that Type I twin boundary is dominant ($v \approx 1$) when the actuation frequency is very low, near the quasi-static case.

Figures 12(a) and 12(c) also indicate that the eddy-current effect is negligible in our tests by the comparison between the best fitting curves of the model including the eddy-current effect (Eq. 9(b)) and that of the model excluding the eddy-current effect (Eq. (10) which can be derived from Eq. 9(b) by setting $q_{eddy} = 0$).

$$\Delta\varepsilon_{\text{stable}} = \frac{\frac{(T_{\text{stable}} - T_0)\cdot\lambda}{t_{\text{h}}}}{2\cdot f_{\text{strain}}\cdot[0.2 - 0.04\cdot v\cdot(T_{\text{stable}} - A_{\text{s}})]} \tag{10}$$

It is seen that the best fitting curves with and without the eddy current overlap and the best fitting values of v are close to each other. Detailed experimental quantification of the eddy current effect and its comparison with the dissipation of martensite reorientation can be found in Appendix B. Therefore, we ignore the eddy current effect in the following analysis. The best fitting of Eq. (10) with the experimental data in Figs. 12(a) and 12(c) gives that $v = 0.65$ for f_{strain} =180 Hz and $v = 0.42$ for f_{strain} = 220 Hz.

It seems in Eq. (10) that the stable strain amplitude $\Delta\varepsilon_{stable}$ is inversely proportional to t_h. But T_{stable} also depends on t_h. As a result, the t_h-dependence of strain amplitude is not inversely proportional, as shown by the comparison between Eq. (10) (with the obtained value $v = 0.65$ and 0.42) and the experimental data in terms of $\Delta\varepsilon_{stable}$ and t_h in Figs. 12(b) and 12(d) for f_{strain} = 180 Hz and 220 Hz respectively.

In summary, the t_h-dependence of the stable strain amplitude in the tests without strain drop (without phase transformation) can be explained by the heat balance between the ambient heat convection and the temperature-dependent energy dissipation of martensite reorientation. The evolution of the effective twinning stress with temperature can be estimated by Eq. (8), in which the fraction v of Type I twin boundary depends on the loading frequency and can be determined by fitting of Eq. (10) with the experimental data. For current system, lowering the loading frequency may lead to an increase in v ($v = 0.65$ for f_{strain} =180 Hz and $v = 0.42$ for f_{strain} = 220 Hz). In an extreme case of quasi-static mechanical test on the specimen, we find that almost all the

nucleated twin boundaries are of Type I (i.e., fraction $v \approx 1$). The measured effective twinning-stress of quasi-static compression at two different temperatures are shown in Fig. 11 (see the two data points of squares within the shaded zone of the Type I twin boundary), indicating the significant temperature dependence. The thick blue line and the thin red line in Fig. 11 represent the temperature dependence of the effective twinning stress (governed by Eq. (8)) in the cases of f_{strain} = 180 Hz and 220 Hz respectively. Here it is assumed that the contribution fraction v of Type I twin boundary relies only on the loading frequency, independent of the temperature or ambient heat-relaxation time t_h.

4.1.2 Region of weak ambient heat exchange (with phase transformation)

We can also use Eq. (10) derived in the previous subsection to describe the t_h-dependence of stable strain amplitude in the tests with weak ambient heat exchange ($t_h > t_h^*$ in Fig. 8) where the stable temperature is always around M_f. In these cases, with the constant stable temperature $T_{stable} = M_f$, Eq. (10) reduces to

$$\Delta\varepsilon_{\text{stable}} = \frac{(M_\text{f} - T_0)\cdot\lambda}{2\cdot t_\text{h}\cdot f_{\text{strain}}\cdot\sigma_{\text{tw}}^{\text{eff}}} \tag{11}$$

where

$$\sigma_{tw}^{\text{eff}} = 0.2 - 0.04\cdot v\cdot(M_\text{f} - A_\text{s}) \tag{12}$$

With M_f -A_s = -6 ^{o}C and v = 0.65 (0.42) for f_{strain} =180 Hz (220 Hz) (determined in Section 4.1.1), we can determine the effective twinning stress by Eq. (12): σ_{tw}^{eff} = 0.36 MPa (0.30 MPa) at f_{strain} = 180 Hz (220 Hz).

Equation (11) shows that the stable strain amplitude is inversely proportional to t_h. The predicted inverse-proportion relation agrees well with the experimental observation in the tests at f_{strain} = 180 Hz and 220 Hz as shown in the Figs. 13(a) and 13(b), respectively. For a better demonstration on the physical meaning of the model, Eq. (11) is normalized as:

$$\Delta\bar{\varepsilon}_{\text{stable}} = \bar{t}_{\text{MR}} \tag{13}$$

where

$$\Delta\bar{\varepsilon}_{\text{stable}} = \frac{\Delta\varepsilon_{\text{stable}}}{\Delta\varepsilon^{\text{complete MR}}}$$

$$\bar{t}_{\text{MR}} = \frac{t_{\text{MR}}}{t_{\text{h}}} = \frac{\left[\dfrac{(M_{\text{f}} - T_0)\cdot\lambda}{2f_{\text{strain}}\cdot\sigma_{\text{tw}}^{\text{eff}}\cdot\Delta\varepsilon^{\text{complete MR}}}\right]}{t_{\text{h}}}$$

The parameter $\Delta\varepsilon^{\text{complete MR}}$ represents the theoretical maximum strain amplitude of the complete martensite reorientation in the whole specimen; it is around 6% based on the lattice parameters of 10M Ni-Mn-Ga specimen. The normalized stable strain amplitude $\Delta\bar{\varepsilon}_{\text{stable}}$ $(=\frac{\Delta\varepsilon_{\text{stable}}}{\Delta\varepsilon^{\text{complete MR}}})$ indicates the fraction of the materials taking martensite reorientation in the specimen. t_{MR} $(=\frac{(M_{\text{f}}-T_0)\cdot\lambda}{2f_{\text{strain}}\cdot\sigma_{\text{tw}}^{\text{eff}}\cdot\Delta\varepsilon^{\text{complete MR}}})$ is the time needed for the energy dissipation of the cyclic complete martensite reorientation to increase the material temperature from T_0 to M_{f} without the ambient heat exchange. The normalized time $\bar{t}_{\text{MR}}$ $(=\frac{t_{\text{MR}}}{t_{\text{h}}})$ is the ratio between the two time scales: t_{MR} and the characteristic heat-relaxation time t_{h}. The time ratio $\bar{t}_{\text{MR}}$ represents the competition between the heat generation from the martensite reorientation and the heat transfer to the ambient, governing the heat balance in the steady states. It is interesting to see in Eq. (13) that the time ratio $\bar{t}_{\text{MR}}$ equals to the material fraction taking martensite reorientation in the specimen, i.e., it governs the fraction of the materials transformed into A-phase in the steady state. The normalized model (Eq. (13)) agrees well with experiments of both loading frequencies in Fig. 13(c).

In summary, the t_{h}-dependence of the stable strain amplitude in the tests with strain drop due to phase transformation is governed by a self-organization process of the specimen: the specimen maintains the stable temperature around M_{f} by adjusting the output strain amplitude (i.e., the fraction of the materials taking martensite reorientation) to keep the balance between the heat generation from martensite reorientation and the

heat transfer to the ambient. For the specimen used in our experiments, its characteristic phase transformation temperatures M_f, M_s, A_s and A_f (35.5 °C, 36.5 °C, 41.5 °C and 42.2 °C respectively) are close to each other. Especially, the difference between M_s and M_f is only 1 °C. So the percentage of Martensite can change from 0% to 100% in this narrow temperature range. That is why the working temperature is almost constant while the output strain (reflecting the percentage of the martensite in the specimen) can change significantly with t_h in the tests of the weak ambient airflows ($t_h > t_h^*$) in Fig. 8.

4.2 Optimal conditions to achieve large stable strain amplitude

The controlled loading conditions in our tests on the FSMA specimen include (1) the magnetic condition (magnetic field frequency f_{mag}), (2) mechanical condition (initial compressive stress σ_{ini}) and (3) thermal condition (the ambient heat convection characterized by the relaxation time t_h). With the systematic data in Table 1 of the tests in the still air, the output strain amplitude of the short- and the long-time actuation at different levels of f_{strain} (= $2f_{mag}$) and σ_{ini} are plotted as contour maps in Figs. 14(a) and 14(b), respectively. In Fig. 14(a), a large $\Delta\varepsilon$ (e.g., $\Delta\varepsilon > 4.5\%$) can be obtained in a proper frequency range, for example, $f_{strain} = 2f_{mag}$ = 140 Hz ~ 220 Hz covering the resonant frequency of the current dynamic system. The resonant frequency depends on the total mass of the specimen and the moving parts of the dynamic system. It also depends on the stiffness of the spring and the specimen. Detailed studies on the mass and the stiffness effects can be found in the literature (Henry et al., 2002; Lai et al., 2008; Techapiesancharoenkij et al., 2011, 2009).

A proper level of the initial stress σ_{ini} is also important to achieve a large $\Delta\varepsilon$. When σ_{ini} is too high (such as 4 MPa), the stress-preferred variant (V1) is always stable and the cyclic martensite reorientation can't occur. In this case $\Delta\varepsilon$ is close to 0 (see $\Delta\varepsilon$ at σ_{ini} = 4 MPa in Table 1). By contrast, if σ_{ini} is too low, the magnetic-field-preferred variant (V2) is stable and cannot fully transform to V1. In this case, $\Delta\varepsilon$ is also small. An interesting phenomenon was found in our experiments at a low level of σ_{ini}, e.g., σ_{ini} =

0.1 MPa in Fig. 15. It's seen that, for a given loading condition, the system does not reach **one** steady state, but switches between **two** "quasi-steady" states. For example, in Fig. 15(a), $\Delta\varepsilon$ switches between 0.4% and 1.3% and the temperature varies correspondingly between 34.1 °C and 37.8 °C. There seems to be two "stable" states switching to each other cyclically. Although some studies on the meta-stability of dynamic behaviors of the traditional SMAs appeared recently in the literature (see (Xia and Sun, 2017, 2015) and the references therein), such phenomenon in FSMAs is observed for the first time and its origin is still unclear and needs further studies.

After choosing proper magnetic field frequency f_{mag} and initial stress σ_{ini}, we need to control the ambient flow (i.e., the heat-relaxation time t_{h}) to avoid the strain drop (avoid phase transformation) in the long-time actuation. As discussed in Section 4.1, there exists an optimal ambient airflow (optimal t_{h}^{*}) at which the stable strain amplitude is maximum and the stable temperature is close to M_{f} (see Fig. 8). From the normalized model of Eq. (13), we can estimate the optimal heat-relaxation time t_{h}^{*} by allowing 100% materials to take the complete martensite reorientation in the whole specimen (i.e., $\Delta\bar{\varepsilon}_{\text{stable}} = 1$):

$$1 = \Delta\bar{\varepsilon}_{\text{stable}} = \bar{t}_{\text{MR}} = \frac{t_{\text{MR}}}{t_{\text{h}}^{*}} = \frac{\left[\dfrac{(M_{\text{f}} - T_0)\cdot\lambda}{\Delta\varepsilon^{\text{complete MR}}\cdot 2\cdot f_{\text{strain}}\cdot\sigma_{\text{tw}}^{\text{eff}}}\right]}{t_{\text{h}}^{*}}$$

$$\Rightarrow t_{\text{h}}^{*} = t_{\text{MR}} = \frac{(M_{\text{f}} - T_0)\cdot\lambda}{\Delta\varepsilon^{\text{complete MR}}\cdot 2\cdot f_{\text{strain}}\cdot\sigma_{\text{tw}}^{\text{eff}}} \tag{14}$$

Equation (14) shows that the stable strain amplitude is maximized when the characteristic heat relaxation time t_{h} equals the characteristic time scale of martensite reorientation t_{MR}. For the given condition: T_0 = 20 °C, M_{f} = 35.5 °C, λ = 4 × 10^6 J·m^{-3}·K^{-1}, $\Delta\varepsilon^{\text{complete MR}}$ = 6%, f_{strain} = 180 Hz (220 Hz), and $\sigma_{\text{tw}}^{\text{eff}}$ = 0.36 MPa (0.30 MPa) determined by Eq. (12) in Section 4.1.2, Eq. (14) predicts the optimal

heat-relaxation time t_h^{*model} = 8.0 s for 180 Hz (7.8 s for 220 Hz). It's seen that, at f_{strain} = 180 Hz, the predicted t_h^{*model} = 8.0 s agrees well with the experimental observation of t_h^* = 8.8 s in Fig. 8(a). But for the case of f_{strain} = 220 Hz, the predicted t_h^{*model} = 7.8 s is not close to the experimental measurement of t_h^* = 11.7 s in Fig. 8(b). The reason for this discrepancy is that Eq. (14) is derived with the assumption of complete martensite reorientation ($\Delta\varepsilon^{complete\ MR}$ = 6%) in the whole specimen. For the case of f_{strain} = 180 Hz which is close to the resonant frequency (see the peak output strain $\Delta\varepsilon_{unstable}$ in Fig. 5), the maximum strain amplitude before the strain drop $\Delta\varepsilon_{unstable}$ = 5.9% in Fig. 5 is close to that of the complete martensite reorientation $\Delta\varepsilon^{complete\ MR}$ = 6%. By contrast, f_{strain} = 220 Hz is far from the resonant frequency (see Fig. 5), and its maximum strain amplitude before the strain drop is $\Delta\varepsilon_{unstable}$ = 3.9%, which is obviously lower than $\Delta\varepsilon^{complete\ MR}$ = 6%. Therefore, we should use the strain amplitude before the strain drop $\Delta\varepsilon_{unstable}$ to replace $\Delta\varepsilon^{complete\ MR}$ in Eq. (14) to estimate t_h^* for the cases far from the resonant frequency of the system.

$$t_h^* = \frac{(M_f - T_0)\cdot\lambda}{\Delta\varepsilon_{unstable}\cdot 2\cdot f_{strain}\cdot\sigma_{tw}^{eff}} \tag{15}$$

Substituting $\Delta\varepsilon_{unstable}$ = 5.9% and 3.9% for the cases of f_{strain} = 180 Hz and 220 Hz respectively into Eq. (15), the predicted t_h^{*model} are 8.1 s and 12.0 s, which agree well with the experimentally observed t_h^* = 8.8 s and 11.7 s in Figs. 8(a) and 8(b), respectively. This implies that, Eq. (14) can be used to find the optimal heat-relaxation time t_h^* for the complete martensite reorientation in the whole specimen with the loading frequency close to the resonant frequency of the system, while Eq. (15) can predict t_h^* for general cases with the reference to the strain amplitude $\Delta\varepsilon_{unstable}$ of the short-time actuation (before the strain drop).

5. Summary and conclusions

In this paper, we performed systematic experiments on the long-time (> 100 s) dynamic behaviors of FSMA under the cyclic magnetic field. The experiments were conducted at various levels of the magnetic field frequency, the initial compressive stress and the ambient airflow velocity. Critical conditions to achieve large stable strain amplitudes in dynamic actuation were derived. We also developed a simple 1D heat transfer model. The analyses from the model well explain the ambient effects on the long-time responses (i.e., the stable strain and the stable temperature) of FSMA observed in the experiments. Furthermore, while the temperature rise caused by the dissipation of the frictional twin boundary motions was generally taken as a negative effect in FSMA actuator applications and should be avoided, we proposed to utilize the temperature rise and the associated heat balance to actively control the stable temperature and the output strain amplitude of FSMA by setting properly the ambient heat exchange condition (i.e., airflow velocity). The important conclusions of the paper are given below:

(1) Energy dissipation due to the high-frequency cyclic martensite reorientation can cause significant temperature rise. When the temperature increases to the characteristic phase transformation temperature, the Martensite-to-Austenite phase transformation will occur in the FSMA specimen, which makes the strain amplitude suddenly decrease to a much lower level. Therefore, the large strain amplitude of FSMA without a steady-state temperature lower than the phase-transformation temperature is at risk of instability (strain drop) during the long-time actuation.

(2) The stable strain amplitude and the stable temperature of FSMA can be controlled by the ambient heat exchange efficiency (corresponding to airflow velocity). The stable strain amplitude depends on the airflow velocity non-monotonically. With the decrease of the airflow velocity (the corresponding heat exchange efficiency decreases), the strain amplitude first increases due to the temperature-dependence of the effective twinning stress and then decreases due to the temperature-induced

phase transformation which disturbs the magnetic-field-induced martensite reorientation. The maximum stable strain amplitude is obtained at the critical heat-relaxation time t_h^* which makes the stable temperature close to (but lower than) the phase-transformation temperature.

(3) A special "isothermal" FSMA actuator with tunable output strain is proposed by taking advantage of the interaction between the temperature-induced phase transformation and the magnetic-field-induced martensite reorientation. The strain amplitude of this actuator changes monotonically with the ambient airflow velocity due to the balance between the heat generated from the martensite reorientation of the untransformed martensite region (related to the strain amplitude) and the heat transferred to the ambient (related to the airflow velocity), while its working temperature is almost constant (close to the phase-transformation temperature) and independent of the strain amplitude. That means, the self-adjustment of the forward and reverse martensitic phase transformations can significantly change the volume fraction of martensite in the specimen (i.e., a significant change of the strain amplitude) within a narrow phase-transformation temperature range.

Acknowledgment

Shaobin Zhang would like to acknowledge China Scholarship Council (CSC) for the financial support (No. 201506280009).

Table 1. The strain amplitudes of all the tests in the still air ambient at different strain frequencies and initial compressive stresses. The strain amplitudes appearing during the short-time actuation (before the strain drop) are highlighted in red.

Strain amplitude $\Delta\varepsilon$ (%)		Strain frequency f_{strain} (Hz)									
		100	120	140	160	180	200	220	240	300	400
Initial stress (MPa)	0.2	**2.3**	2.2 ↘ **1.8**	2.6 ↘ **1.5**	4.2 ↘ **1.1**	4.7 ↘ **1.3**	3.7 ↘ **1.2**	3.3 ↘ **1.0**	2.6 ↘ **1.0**	1.1 ↘ **0.4**	1.0 ↘ **0.2**
	0.4	4.2 ↘ **1.3**	4.3 ↘ **1.2**	4.5 ↘ **1.4**	5.2 ↘ **1.2**	5.9 ↘ **1.0**	4.7 ↘ **1.2**	3.9 ↘ **1.0**	2.9 ↘ **1.0**	1.7 ↘ **0.6**	1.1 ↘ **0.4**
	1.0	2.6 ↘ **1.1**	2.8 ↘ **0.8**	3.1 ↘ **0.9**	4.1 ↘ **0.7**	4.4 ↘ **1.2**	5.6 ↘ **0.8**	4.3 ↘ **0.7**	3.8 ↘ **0.6**	2.1 ↘ **0.6**	1.2 ↘ **0.4**
	1.8	**0.8**	**0.8**	**0.5**	**0.5**	**0.5**	**0.6**	**0.6**	**0.5**	0.9 ↘ **0.5**	2.0 ↘ **0.5**
	4.0	**0.2**	**0.2**	**0.1**	**0.2**	**0.3**	**0.1**	**0.1**	**0.1**	**0.2**	**0.2**

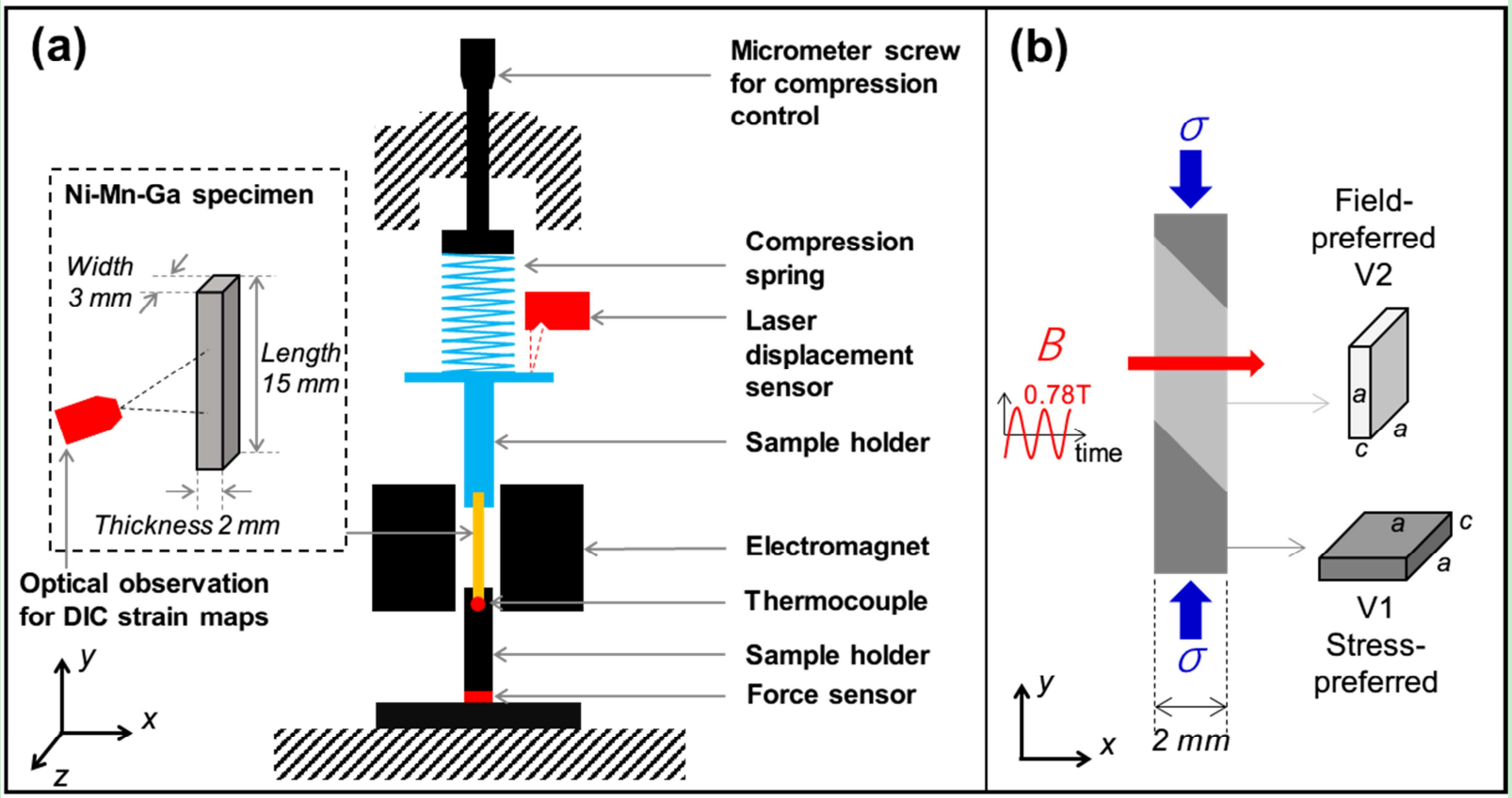

Figure 1. (a) Schematic of actuation system to achieve high-frequency cyclic martensite reorientation, where the fixed parts (immobile components) during the dynamic actuation are in black, the moving parts (the spring and the upper sample holder) are in blue and the measuring sensors are in red. (b) Schematic of the martensite reorientation between the stress-preferred variant (V1) and the magnetic-field-preferred variant (V2) in Ni-Mn-Ga specimen under the magneto-mechanical actuation. Approximated tetragonal martensite variant of one short axis (*c*-axis) and two long axes (*a*-axis) are adopted and the difference between *a* and *c* is shown exaggeratedly here.

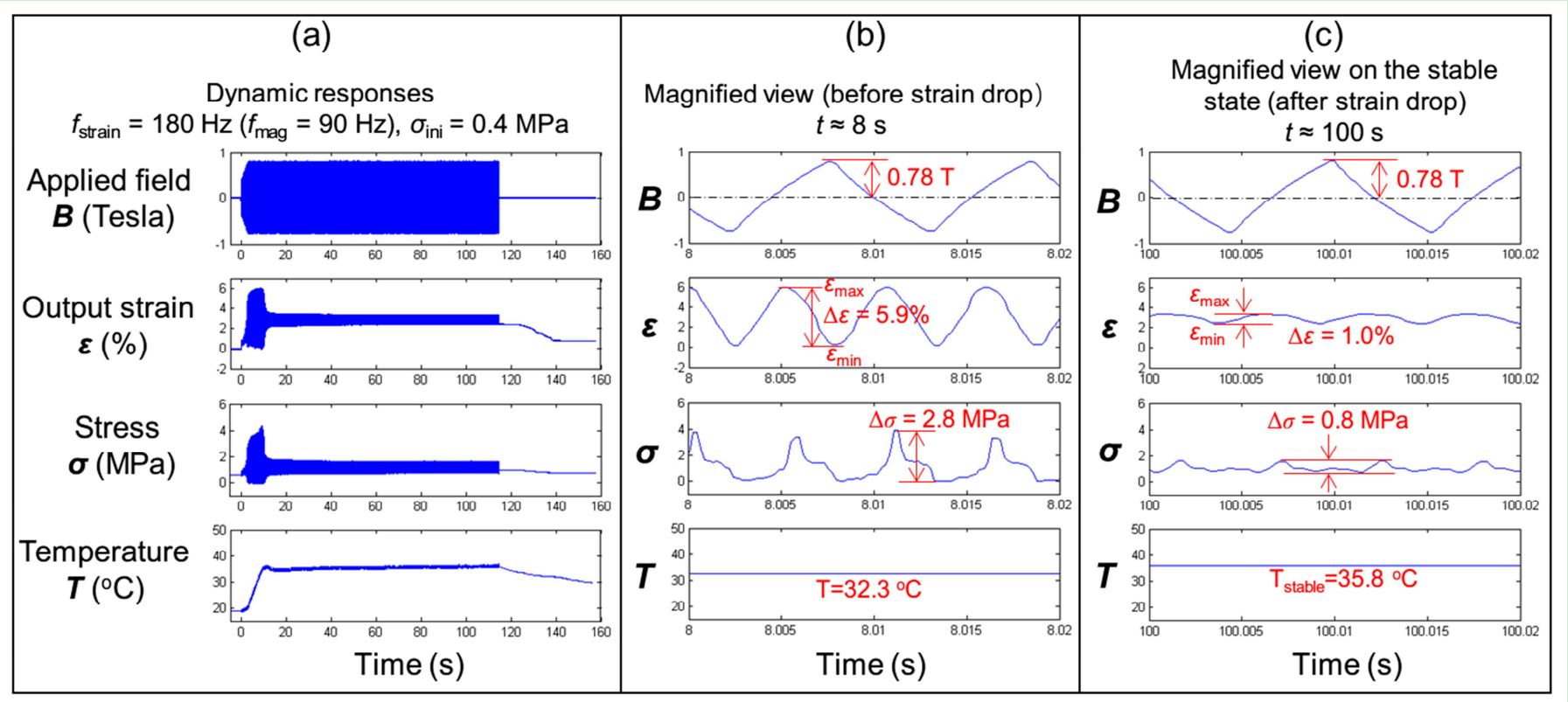

Figure 2. Typical responses of strain, stress and temperature of Ni-Mn-Ga specimen under long-time actuation (> 100 s) at the strain frequency f_{strain} = 180 Hz (f_{mag} = 90 Hz): (a) full-time responses, (b) magnified view of the responses at $t \approx 8$ s (before strain drop) and (c) stable state at $t \approx 100$ s (after the strain drop). (d) and (e) are the local-strain fields at the maximum nominal strain ε_{max} and the minimum one ε_{min} for the two typical instants (before and after the strain drop) corresponding to the nominal behaviors shown in (b) and (c), respectively; the strain profiles along the centerline of the specimen are plotted in terms of $\varepsilon_{yy\text{-}centerline}$ by red lines.

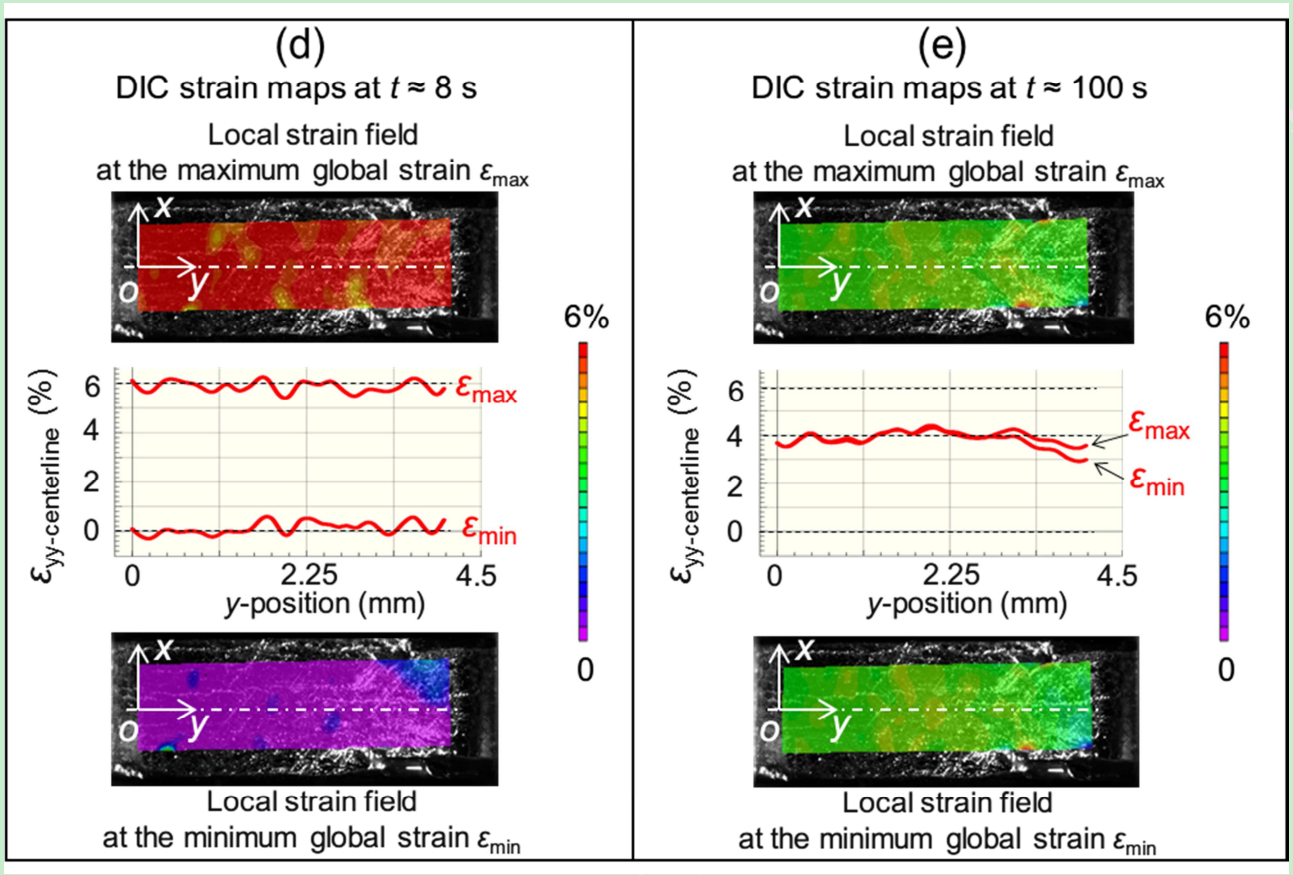

Figure 2. (Continue)

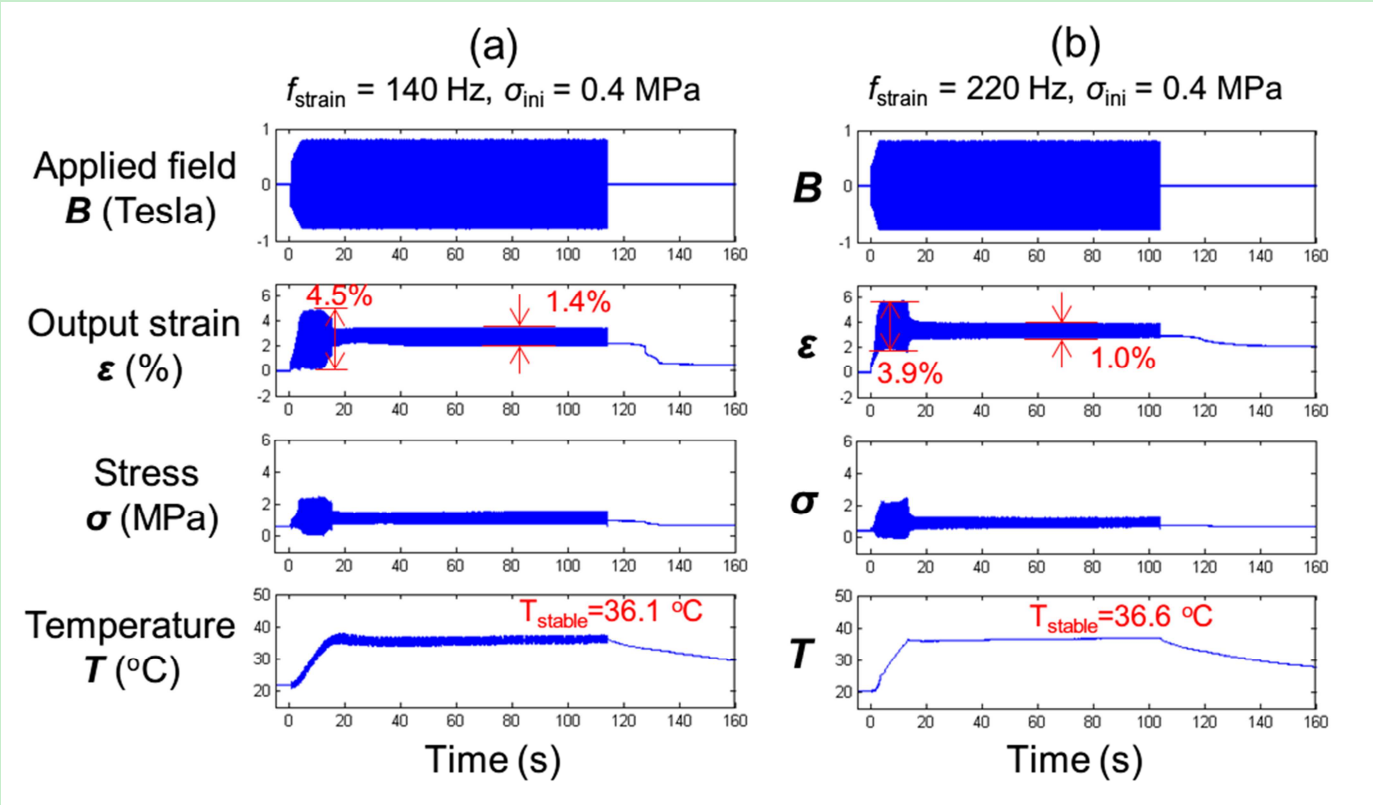

Figure 3. Typical responses of the Ni-Mn-Ga specimen under the same initial compressive stress σ_{ini} = 0.4 MPa with different frequency: (a) f_{strain} = 140 Hz (f_{mag} = 70 Hz) and (b) f_{strain} = 220 Hz (f_{mag} = 110 Hz).

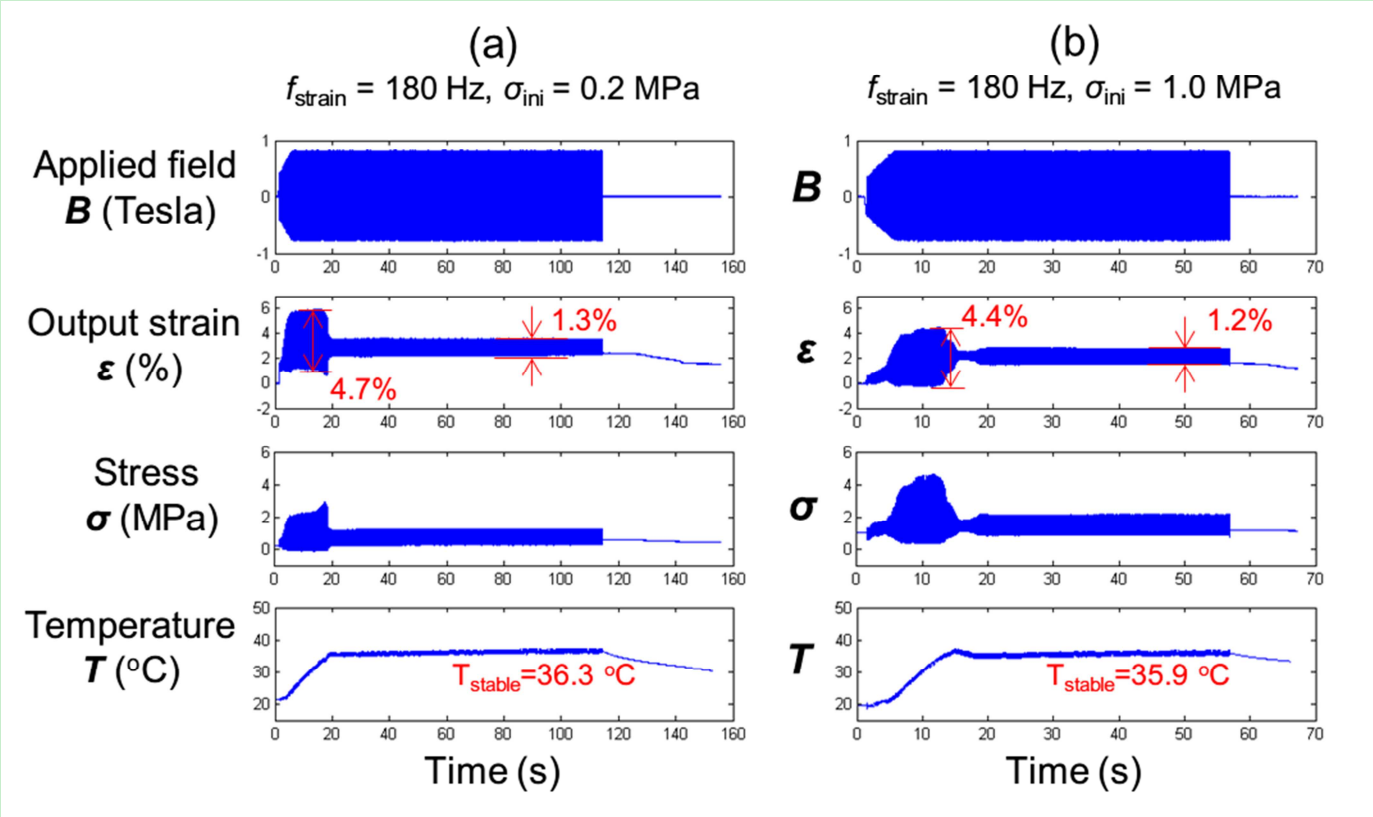

Figure 4. Typical responses of Ni-Mn-Ga under the same frequency f_{strain} = 180 Hz (f_{mag} = 90 Hz) with different initial compressive stress: (a) σ_{ini} = 0.2 MPa and (b) σ_{ini} = 1.0 MPa.

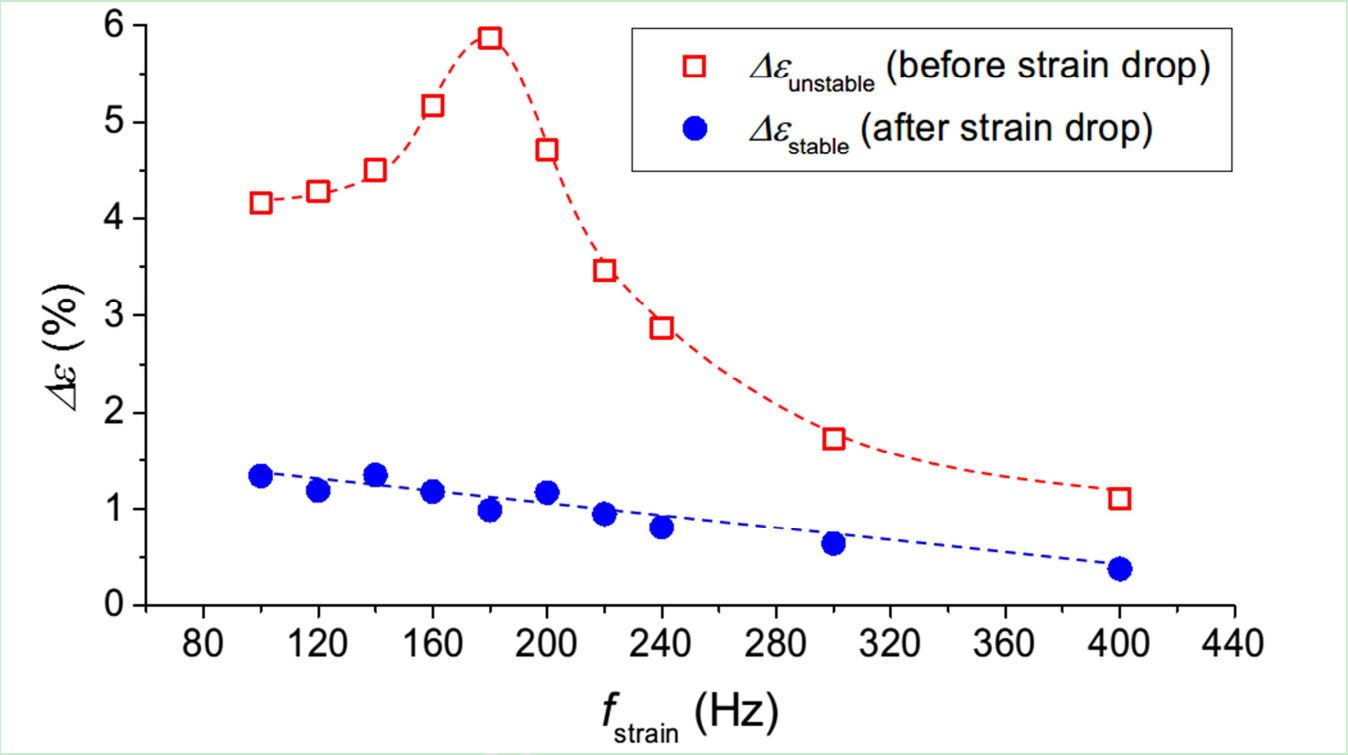

Figure 5. The frequency-dependent stable and unstable strain amplitudes of the tests with the initial compressive stress σ_{ini} = 0.4 MPa in still air. $\Delta\varepsilon_{unstable}$ and $\Delta\varepsilon_{stable}$ represent the strain amplitudes of the short-time actuation (before strain drop) and the long-time actuation (after strain drop), respectively. The dashed lines are for guiding eyes.

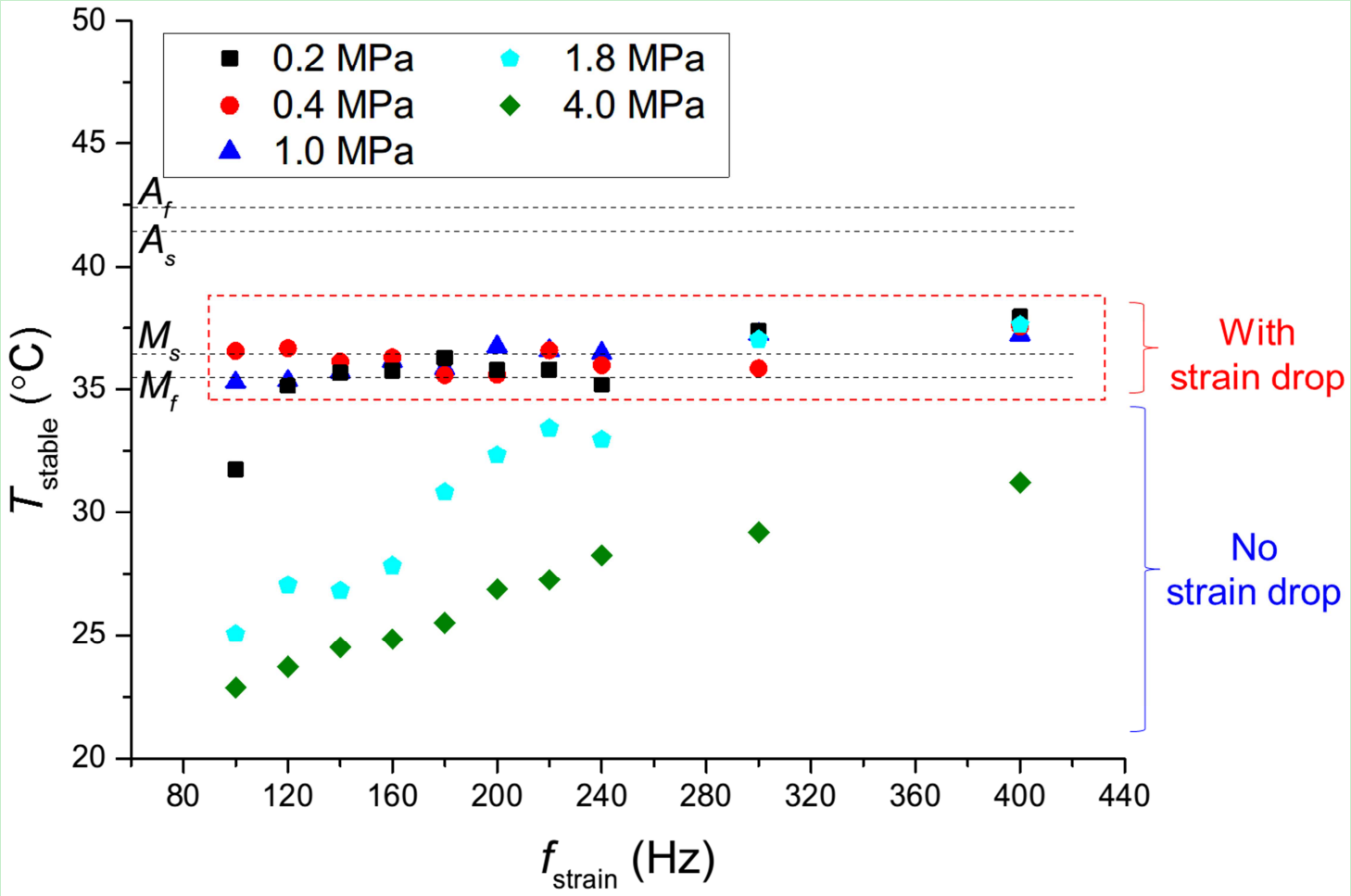

Figure 6. Stable temperatures T_{stable} of all tests conducted in still air with different loading conditions (different strain frequencies and initial compressive stresses). The cases with strain drop are marked by the red dashed rectangle.

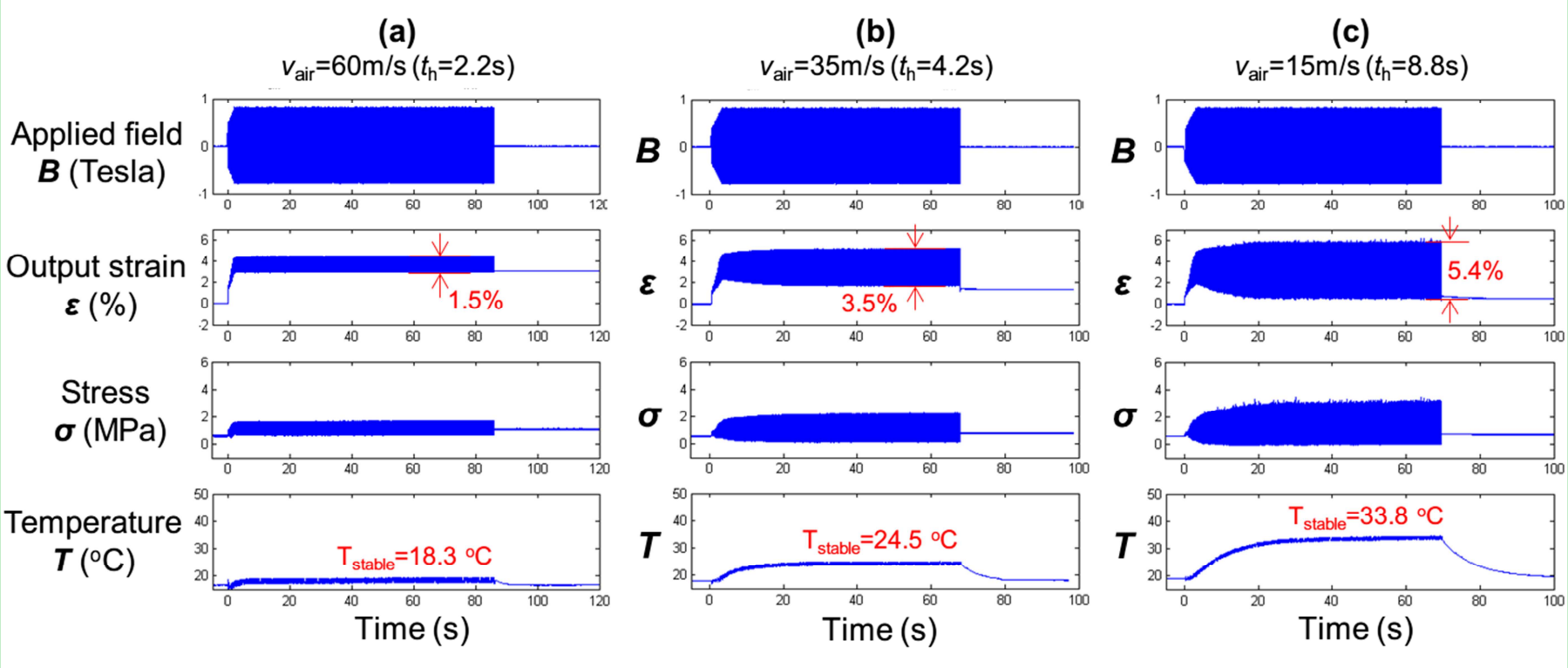

Figure 7. The responses of the tests at different levels of ambient airflow velocity: (a) ~ (f) are respectively for the air velocity V_{air} = 60 m/s (t_h = 2.2 s), 35 m/s (t_h = 4.2 s), 15 m/s (t_h = 8.8 s), 8 m/s (t_h = 14.0 s), 3 m/s (t_h = 22.2 s) and 0 m/s (t_h = 68.9 s). All the tests are conducted at the same magneto-mechanical loading conditions of f_{strain} = 180 Hz (f_{mag} = 90 Hz) and σ_{ini} = 0.4 MPa.

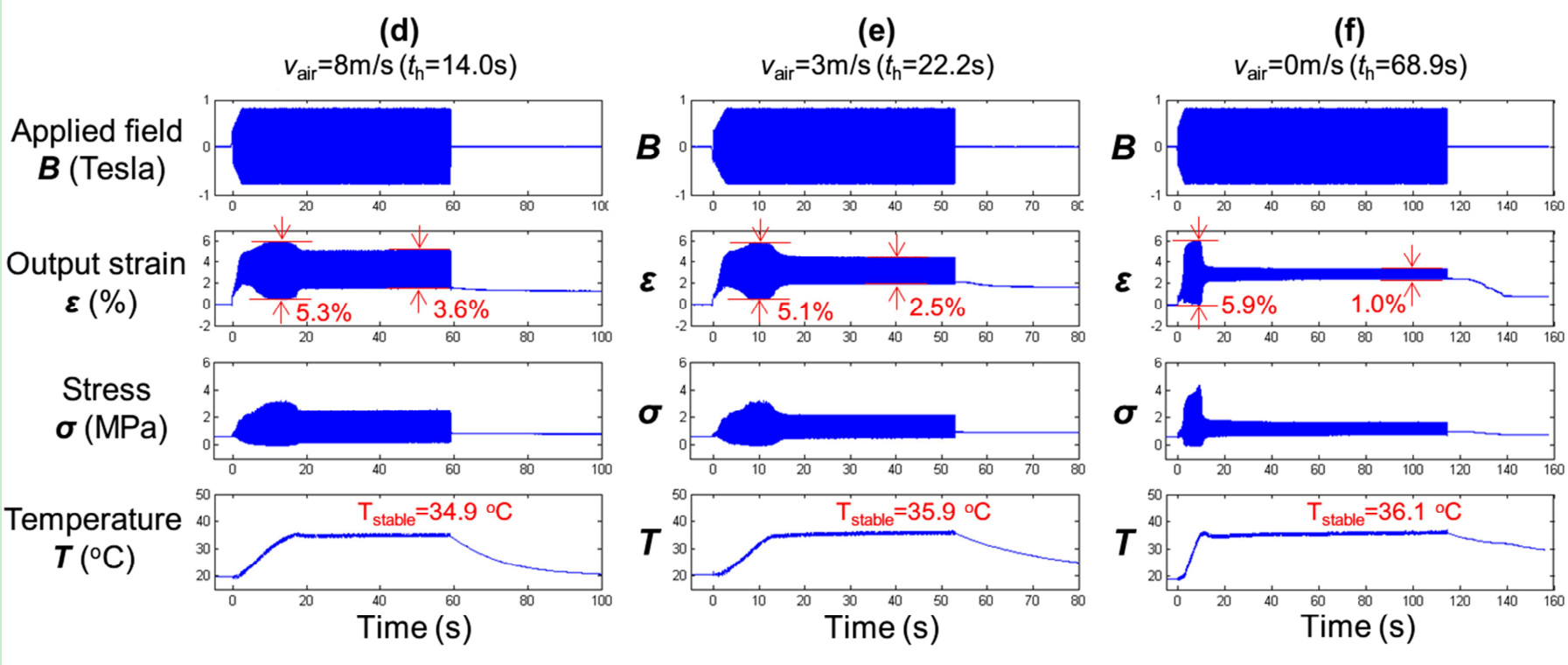

Figure 7. (Continue)

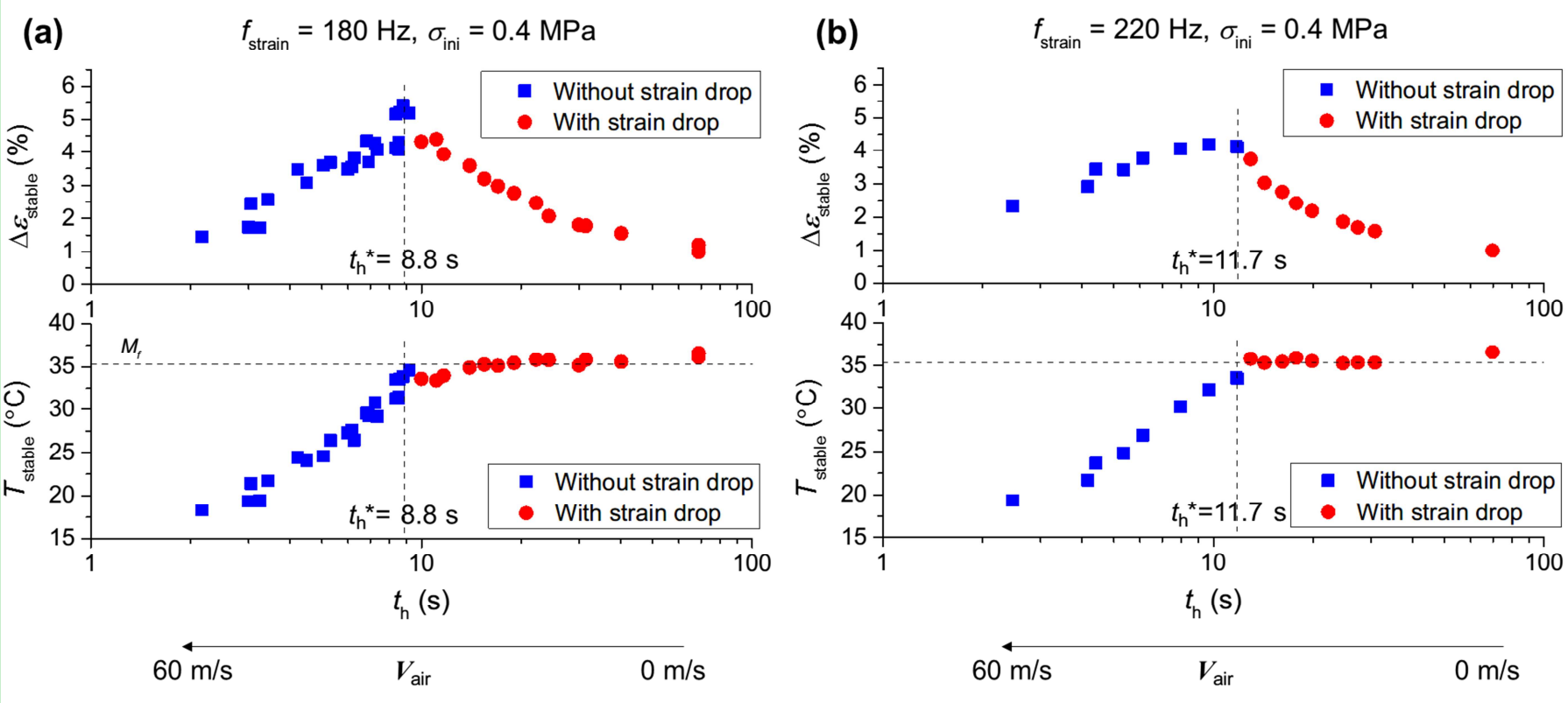

Figure 8. Airflow-dependence (t_h-dependence) of the stable strain amplitude $\Delta\varepsilon_{stable}$ and the stable temperature T_{stable} for all the tests with ambient airflow of different velocities for the two typical loading frequencies: (a) f_{strain} = 180 Hz and (b) f_{strain} = 220 Hz.

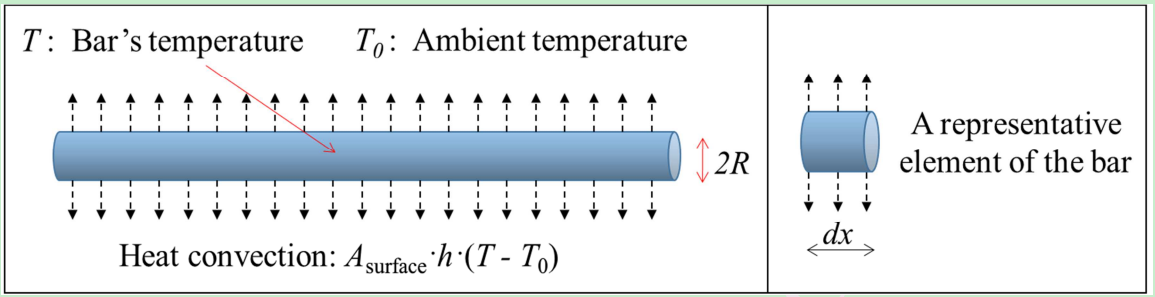

Figure 9. One-dimensional heat-transfer model

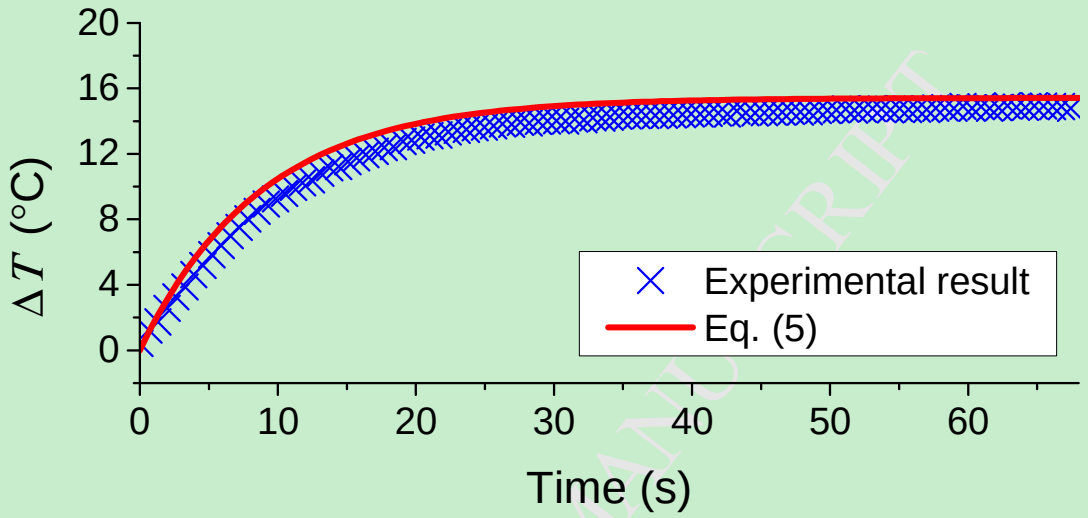

Figure 10. Comparison of the temperature rise between Eq. (5) and the experimental data from the test of f_{strain} = 180 Hz, σ_{ini} = 0.4 MPa and V_{air} = 15m/s (t_h = 8.8s), whose responses of the strain and the stress can be found in Fig. 7(c).

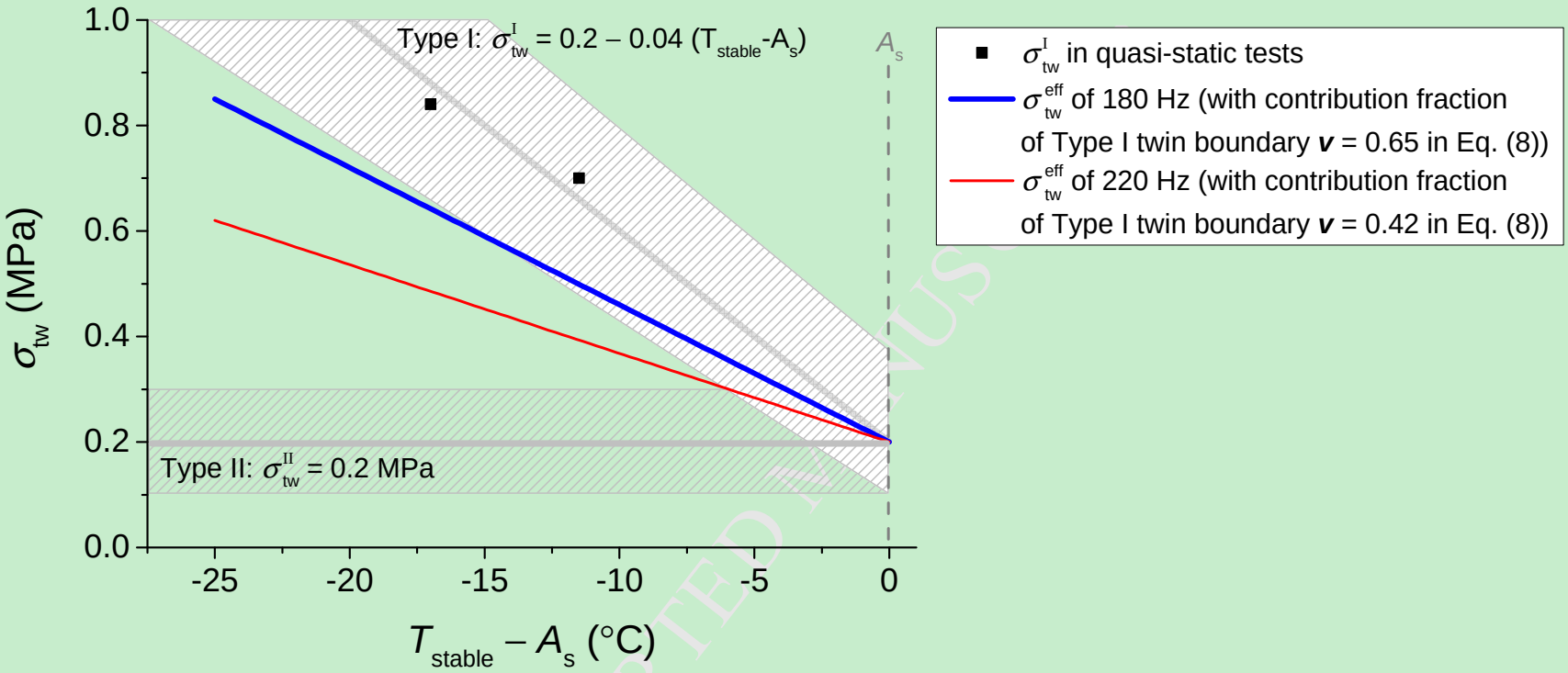

Figure 11. The temperature dependence of twinning stress for the twin boundary motion during the magneto-mechanically driven martensite reorientation. The two shaded regions represent the temperature dependences of the twinning stresses of the Type I and Type II twin boundaries, respectively, reported in (Heczko and Straka, 2003; Soroka et al., 2018; Sozinov et al., 2017; Straka et al., 2012; Zreihan et al., 2016). The thick blue and thin red lines (determined by Eq. (8) with v = 0.65 and 0.42 respectively) represent the temperature dependences of the effective twinning stress of the mixed Type I and Type II twin boundaries in the dynamic actuation of f_{strain} = 180 Hz and f_{strain} = 220 Hz, respectively.

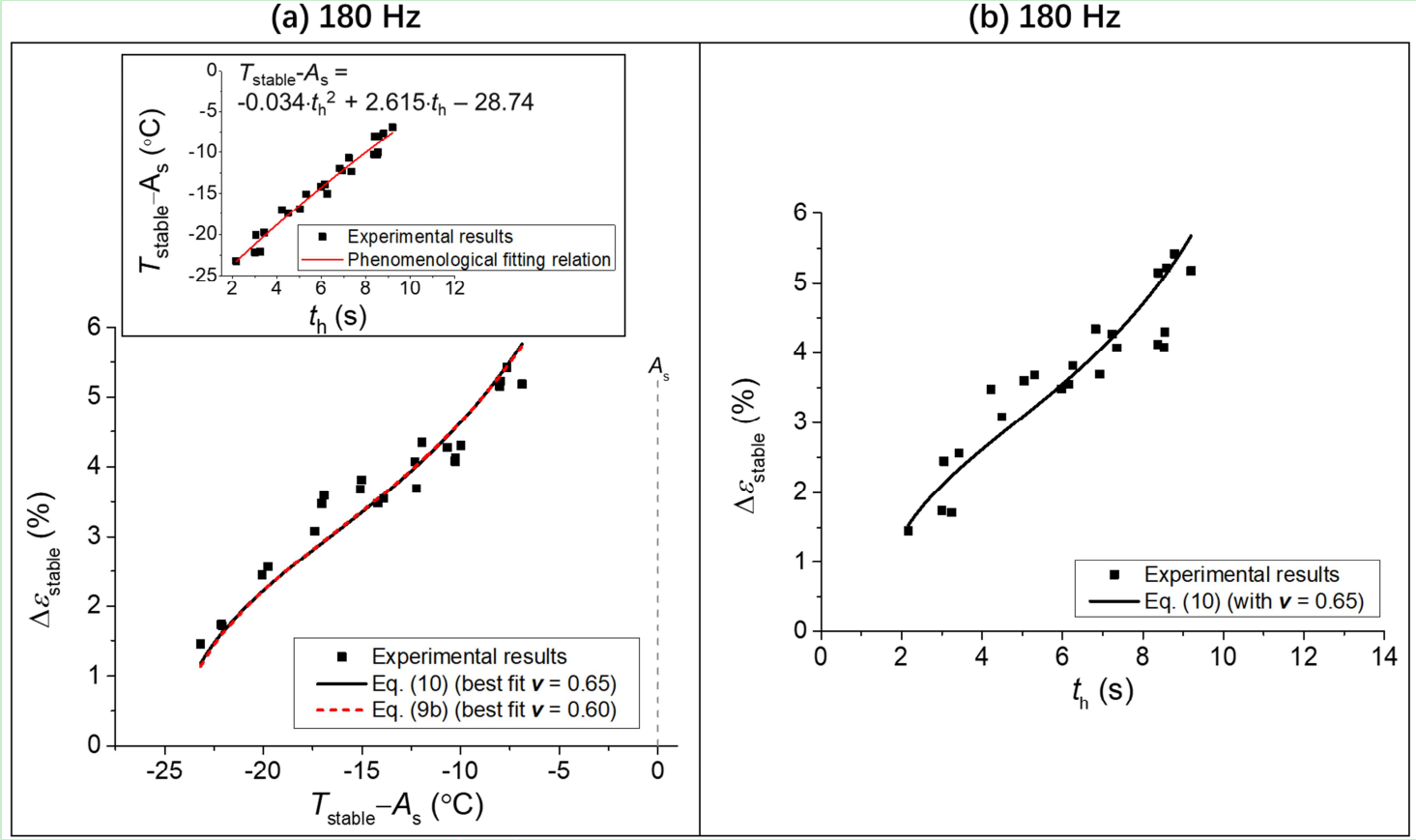

Figure 12. Comparison between the experiments (from the tests without strain drop ($t_h < t_h^*$) in Fig. 8) and the model (Eq. (9b) and Eq. (10) with and without considering eddy-current effect respectively) to estimate the contribution fraction ($\boldsymbol{\nu}$) of Type I twin boundary during the dynamic martensite reorientation process. (a) and (b) are respectively the dependences of stable strain amplitude $\Delta\varepsilon_{stable}$ on (T_{stable}-A_s) and t_h at f_{stain} = 180 Hz; (c) and (d) are respectively the dependences of stable strain amplitude $\Delta\varepsilon_{stable}$ on (T_{stable}-A_s) and t_h at f_{stain} = 220 Hz. The relations between (T_{stable}-A_s) and t_h are plotted in the insets of (a) and (c).

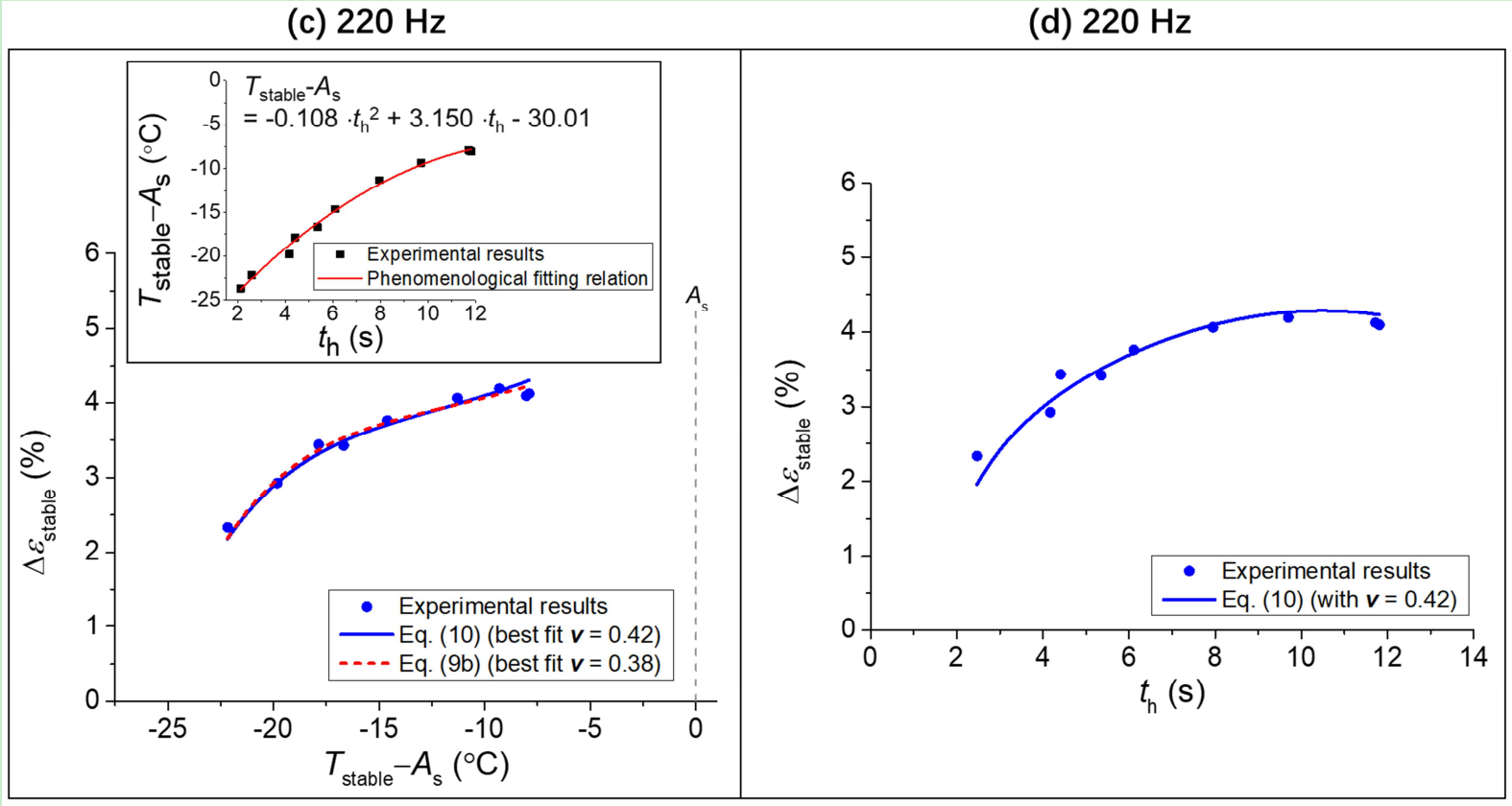

Figure 12. (Continue)

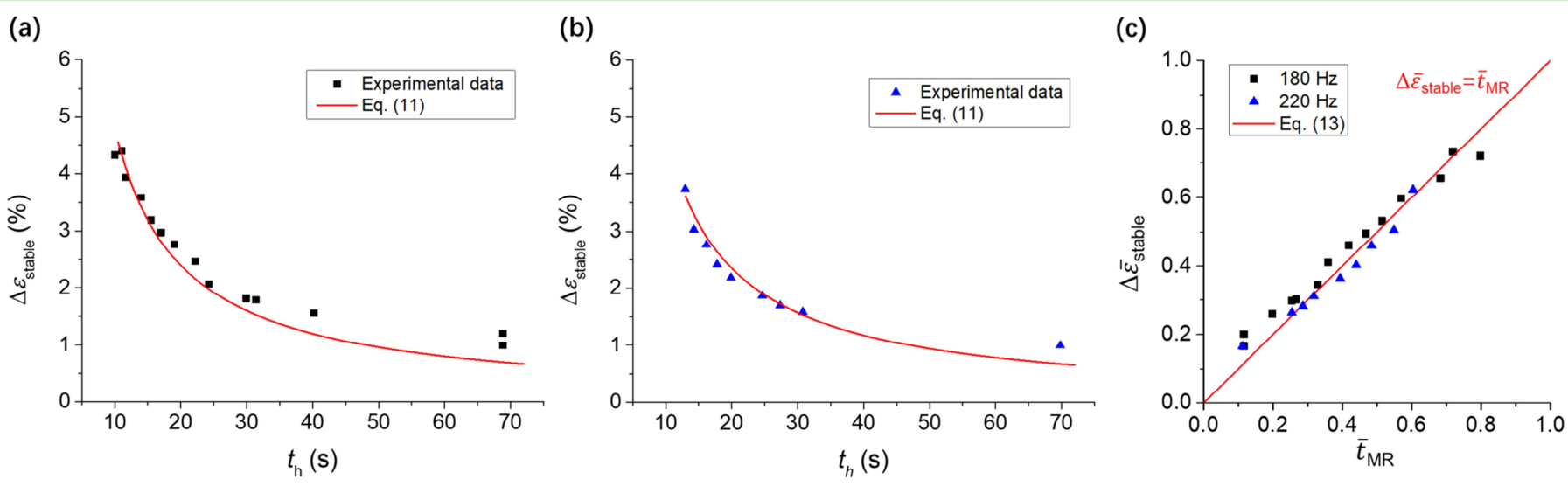

Figure 13. The comparison between the theoretical model (Eq. (11)) and the experimental data for the tests at f_{strain} = 180 Hz (a) and 220 Hz (b). (c) The comparison between the normalized model (Eq. (13)) and the normalized experimental data of f_{strain} = 180 and 220 Hz in terms of $\Delta\bar{\varepsilon}_{stable}$ and $\bar{t}_{MR}$.

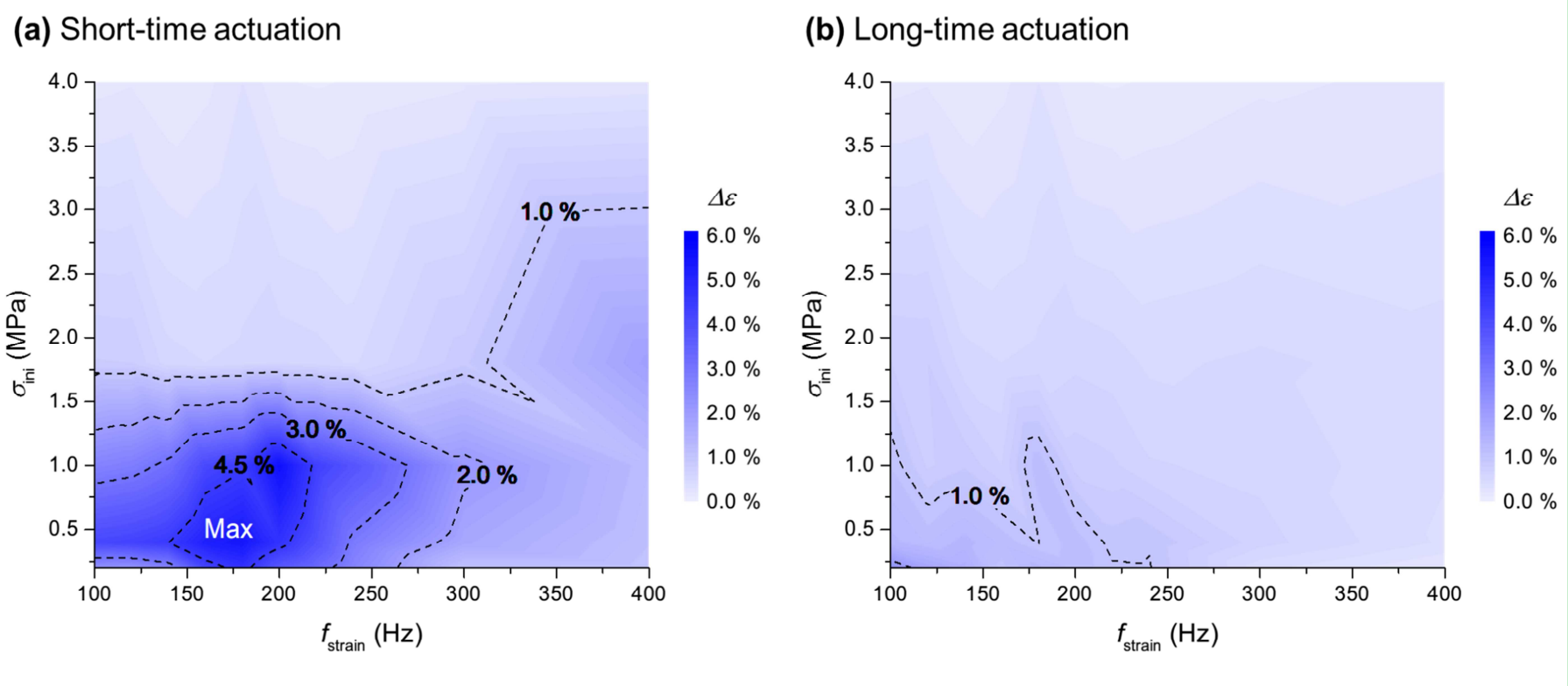

Figure 14. Contours of the output strain amplitude $\Delta\varepsilon$ at various frequencies and initial compressive stresses during the short-time actuation (a) and the long-time actuation (b). The data are from Table 1 and all the tests are conducted in the still air.

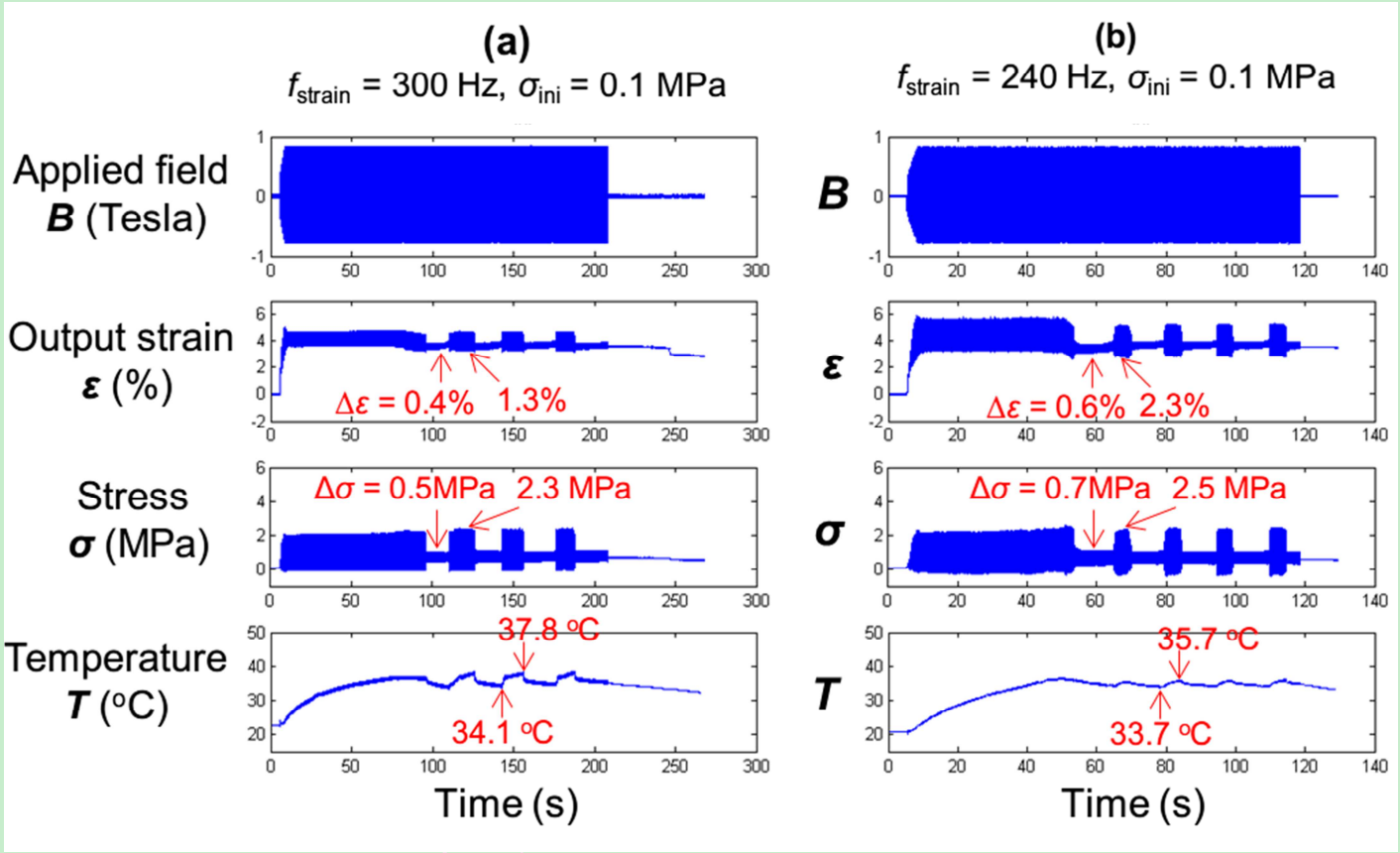

Figure 15. Oscillation phenomenon observed in the tests at the low initial compressive stress σ_{ini} = 0.1 MPa: the strain amplitude $\Delta\varepsilon$ and the stress amplitude $\Delta\sigma$ periodically switch between two “stable” states.

Appendix A

Determination of the characteristic heat-relaxation time t_h

The specimen is held between two electromagnet poles during the tests and heated due to high-frequency cyclic martensite reorientation. To determine the characteristic heat-relaxation time t_h, the evolution of the specimen temperature after the applied magnetic field is turned off is measured in a constant ambient airflow. So there is no heat generation in the specimen and the temperature relaxation is only due to the heat convection. The value of the heat-relaxation time t_h is determined by fitting the experimental cooling curve with an exponential equation $T = T_{\text{room}} + (T_0 - T_{\text{room}}) \cdot e^{-\frac{t}{t_h}}$, which describes the heat-convection relaxation (He et al., 2010; He and Sun, 2010). For example, in Fig. A1, the value of t_h at the ambient airflow velocity of 15 m/s is determined to be 8.8 s. By using this method, t_h at different ambient conditions can be experimentally measured.

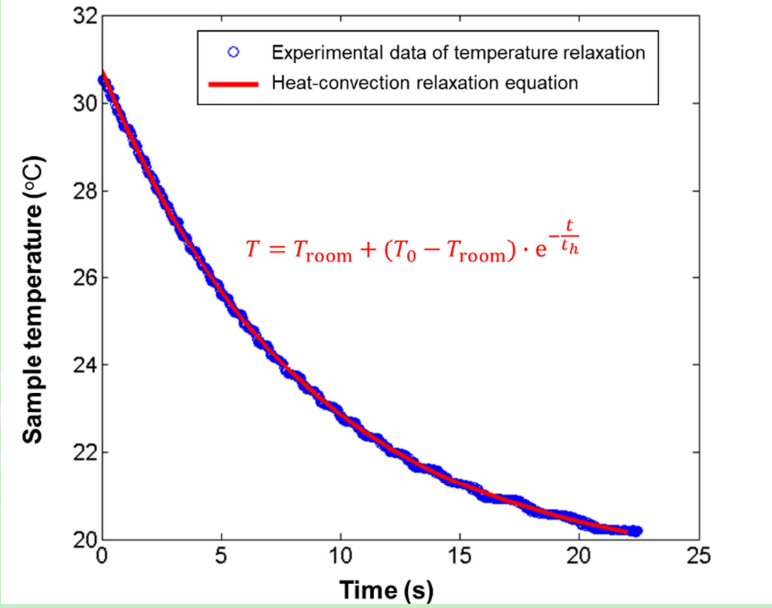

Figure A1. Temperature relaxation of Ni-Mn-Ga single crystal sample (2×3×15 mm) under the ambient airflow of 15 m/s. The fitted characteristic heat-relaxation time t_h is 8.8 s.

Appendix B

Measurement of the heat release from eddy current

The temperature rise during the dynamic actuation of FSMA is attributed to both the energy dissipation of the frictional twin boundary motion and the eddy current (Henry 2002; Lai 2009). In order to quantify and compare the contributions from these two mechanisms separately, we conducted the tests with different initial stresses as shown in Fig. B1. When the initial compressive stress σ_{ini} = 0.4 MPa (Fig. B1(a)), the strain amplitude is large ($\Delta\varepsilon$ = 5.9% at actuation time t = 0 ~ 10 s) and the temperature increases rapidly (with the increasing rate around 1.6 ^{o}C/s). By contrast, when σ_{ini} = 4.0 MPa (which is larger than the so-called "blocking stress" (Heczko et al., 2000)), the output strain amplitude is zero (i.e., no martensite reorientation) as shown in Fig. B1(b) where the temperature rise purely induced by the eddy current is very slow. The temperature increasing rate is around 0.04 ^{o}C/s at t = 0 ~ 10 s, which is much smaller than that with the large $\Delta\varepsilon$ from martensite reorientation in Fig. B1(a).

Similar to the test in Fig. B1(b) showing the eddy-current effect, we did more tests of different frequencies with the same initial stress σ_{ini} = 4.0 MPa. The frequency dependence of the eddy-current induced temperature rise after 100 s actuation $\Delta T_{\text{eddy}}^{100s}$ is shown in Fig. B2(a). As the material specific heat capacity per unit volume λ = 4 × 10^6 J·m^{-3}·K^{-1}, the heat release rate due to the eddy current can be determined (from Eq. (5) by setting q_{TB} = 0) as

$$q_{\text{eddy}} = \frac{\Delta T_{\text{eddy}}^{100s} \cdot \lambda}{t_{\text{h}} \cdot \left(1 - e^{-\frac{100}{t_{\text{h}}}}\right)} \quad (\text{J} \cdot \text{m}^{-3} \cdot \text{s}^{-1}) \tag{B1}$$

where the characteristic heat-relaxation time t_h is 68.9 s in the still air. Figure B2(b) summarizes the frequency dependence of q_{eddy}, which is approximately fitted by a linear

relation $q_{\text{eddy}} = 2320.7 \cdot f_{strain} - 1.35 \times 10^5$ ($\text{J}\cdot\text{m}^{-3}\cdot\text{s}^{-1}$) in the strain frequency range [100 Hz, 400 Hz].

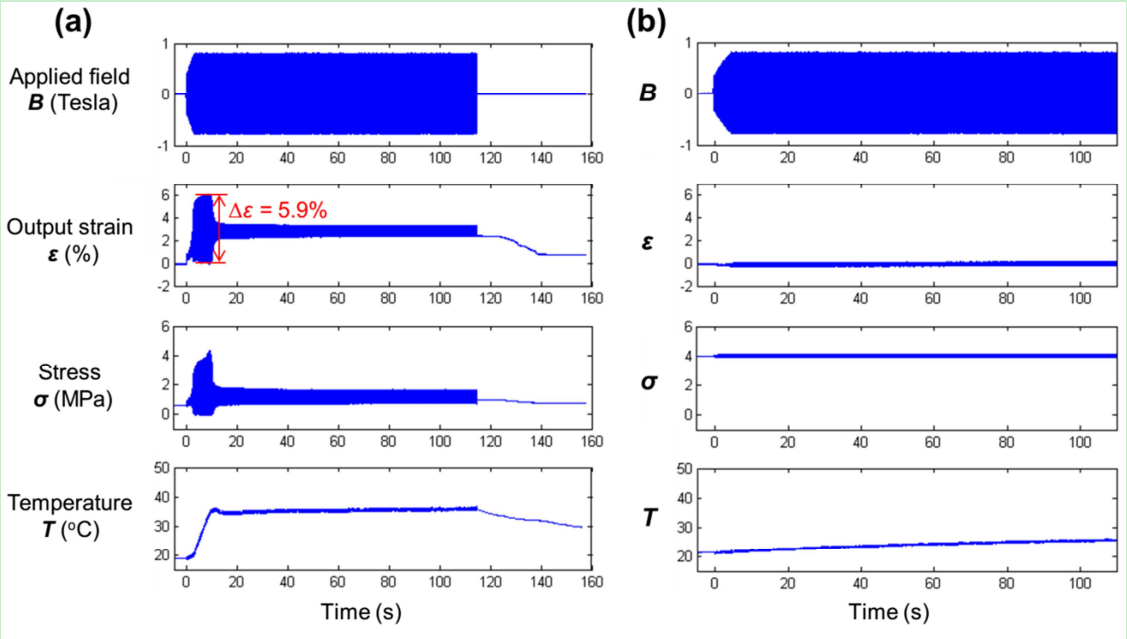

Figure B1. Typical tests to compare the temperature rises induced by the martensite-reorientation dissipation and the eddy current at the strain frequency f_{strain} =180 Hz, with the different initial compressive stresses: (a) 0.4 MPa and (b) 4.0 MPa.

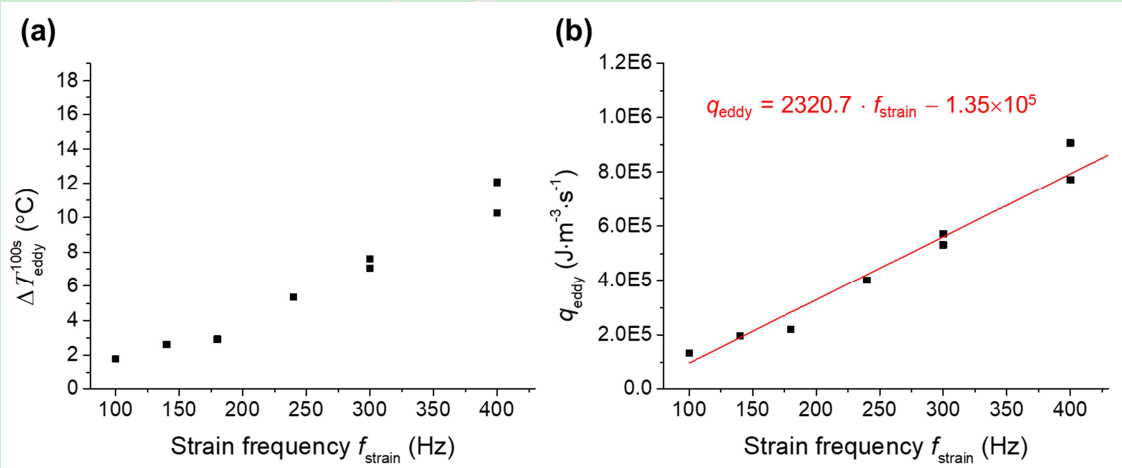

Figure B2. The temperature rise due to eddy current after the actuation of 100 s at different strain frequencies f_{strain} are shown in (a) and the corresponding heat generation rate is shown in (b).

References

Aaltio, I., Lahelin, M., Söderberg, O., Heczko, O., Löfgren, B., Ge, Y., Seppälä, J., Hannula, S.P., 2008. Temperature dependence of the damping properties of Ni-Mn-Ga alloys. Mater. Sci. Eng. A 481–482, 314–317. doi:10.1016/j.msea.2006.12.229

Adachi, Y., Ogi, Y., Kobayashi, N., Hayasaka, Y., Kanomata, T., Rie, Y., 2017. Temperature Dependences of the Electrical Resistivity on the Heusler Alloy System. Metals (Basel). 7. doi:10.3390/met7100413

Arndt, M., Griebel, M., Novák, V., Roubíček, T., Šittner, P., 2006. Martensitic transformation in NiMnGa single crystals: Numerical simulation and experiments. Int. J. Plast. 22, 1943–1961. doi:10.1016/j.ijplas.2006.03.001

Asua, E., García-Arribas, A., Etxebarria, V., Feuchtwanger, J., 2014. Pulsed-mode operation and performance of a ferromagnetic shape memory alloy actuator. Smart Mater. Struct. 23, 25023. doi:10.1088/0964-1726/23/2/025023

Auricchio, F., Bonetti, E., Scalet, G., Ubertini, F., 2014. Theoretical and numerical modeling of shape memory alloys accounting for multiple phase transformations and martensite reorientation. Int. J. Plast. 59, 30–54. doi:10.1016/j.ijplas.2014.03.008

Basaran, B., 2009. Magnetic Field-Induced Phase Transformation and Power Harvesting Capabilities in Magnetic Shape Memory Alloys. PhD thesis, Texas A&M University, USA.

Bhattacharya, K., 2003. Microstructure of martensite : why it forms and how it gives rise to the shape-memory effect. Oxford University Press.

Blanter, M.S., Golovinm, I.S., Neuhauser, H., Sinning, H.R., 2007. Internal friction in metallic materials : a handbook. Springer, Berlin Heidelberg.

Brinson, L.C., Schmidt, I., Lammering, R., 2004. Stress-induced transformation behavior of a polycrystalline NiTi shape memory alloy: Micro and macromechanical investigations via in situ optical microscopy. J. Mech. Phys. Solids 52, 1549–1571. doi:10.1016/j.jmps.2004.01.001

Bruno, N.M., Wang, S., Karaman, I., Chumlyakov, Y.I., 2016. Reversible Martensitic Transformation under Low Magnetic Fields in Magnetic Shape Memory Alloys. Sci Rep 1–10. doi:10.1038/srep40434

Bruno, O.P., Leo, P.H., Reitich, F., 1995. Free Boundary Conditions at Austenite-Martensite Interfaces. Phys. Rev. Lett. 74, 746–749.

Chen, X., He, Y., Moumni, Z., 2013. Twin boundary motion in NiMnGa single crystals under biaxial compression. Mater. Lett. 90, 72–75. doi:10.1016/j.matlet.2012.08.107

Chen, X., Moumni, Z., He, Y., Zhang, W., 2014. A three-dimensional model of magneto-mechanical behaviors of martensite reorientation in ferromagnetic shape memory alloys. J. Mech. Phys. Solids 64, 249–286. doi:10.1016/j.jmps.2013.11.005

Chmielus, M., Chernenko, V.A., Knowlton, W.B., Kostorz, G., Müllner, P., 2008. Training, constraints, and high-cycle magneto-mechanical properties of Ni-Mn-Ga magnetic shape-memory alloys. Eur. Phys. J. Spec. Top. 158, 79–85. doi:10.1140/epjst/e2008-00657-3

Chulist, R., Straka, L., Lanska, N., Soroka, A., Sozinov, A., Skrotzki, W., 2013. Characterization of mobile type I and type II twin boundaries in 10M modulated Ni-Mn-Ga martensite by electron backscatter diffraction. Acta Mater. 61, 1913–1920. doi:10.1016/j.actamat.2012.12.012

Cisse, C., Zaki, W., Ben Zineb, T., 2016. A review of constitutive models and modeling techniques for shape memory alloys. Int. J. Plast. 76, 244–284. doi:10.1016/j.ijplas.2015.08.006

Cui, Y., Li, Y., Wang, Z., Lei, Q., Koizumi, Y., Chiba, A., 2017. Regulating twin boundary mobility by annealing in magnesium and its alloys. Int. J. Plast. 99, 1–18. doi:10.1016/j.ijplas.2017.08.002

Dai, Y., Hou, L., Fautrelle, Y., Li, Z., Esling, C., Ren, Z., Li, X., 2018. Detwinning process of martensite in $Ni_{58}Mn_{25}Ga_{17}$ as a high temperature shape memory alloy under uniaxial compression. Int. J. Plast. 103, 203–213. doi:10.1016/j.ijplas.2018.01.013

Faran, E., Riccardi, L., Shilo, D., 2017. Inertia-Controlled Twinning in Ni–Mn–Ga Actuators: A Discrete Twin-Boundary Dynamics Study. Shape Mem. Superelasticity 3, 206–217. doi:10.1007/s40830-017-0112-5

Faran, E., Shilo, D., 2016. A discrete twin-boundary approach for simulating the magneto-mechanical response of Ni–Mn–Ga. Smart Mater. Struct. 25, 95020. doi:10.1088/0964-1726/25/9/095020

Franco, V., Conde, A., 2012. Magnetic refrigerants with continuous phase transitions : Amorphous and nanostructured materials. Scr. Mater. 67, 594–599. doi:10.1016/j.scriptamat.2012.05.004

Glavatska, N., Mogylny, G., Glavatskiy, I., Gavriljuk, V., 2002. Temperature stability of martensite and magnetic field induced strain in Ni-Mn-Ga. Scr. Mater. 46, 605–610. doi:10.1016/S1359-6462(02)00019-2

Haldar, K., Lagoudas, D.C., Karaman, I., 2014. Magnetic field-induced martensitic phase transformation in magnetic shape memory alloys: Modeling and experiments. J. Mech. Phys. Solids 69, 33–66. doi:10.1016/j.jmps.2014.04.011

He, Y., Yin, H., Zhou, R., Sun, Q., 2010. Ambient effect on damping peak of NiTi shape memory alloy. Mater. Lett. 64, 1483–1486. doi:10.1016/j.matlet.2010.03.068

He, Y.J., Chen, X., Moumni, Z., 2012. Reversible-strain criteria of ferromagnetic shape memory alloys under cyclic 3D magneto-mechanical loadings. J. Appl. Phys. 112, 33902. doi:10.1063/1.4739711

He, Y.J., Chen, X., Moumni, Z., 2011. Two-dimensional analysis to improve the output stress in ferromagnetic shape memory alloys. J. Appl. Phys. 110, 63905. doi:10.1063/1.3636366

He, Y.J., Sun, Q.P., 2011. On non-monotonic rate dependence of stress hysteresis of superelastic shape memory alloy bars. Int. J. Solids Struct. 48, 1688–1695. doi:10.1016/j.ijsolstr.2011.02.017

He, Y.J., Sun, Q.P., 2010. Rate-dependent domain spacing in a stretched NiTi strip. Int. J. Solids Struct. 47, 2775–2783. doi:10.1016/j.ijsolstr.2010.06.006

Heczko, O., Cejpek, P., Drahokoupil, J., Holý, V., 2016. Structure and microstructure of Ni-Mn-Ga single crystal exhibiting magnetic shape memory effect analysed by high resolution X-ray diffraction. Acta Mater. 115, 250–258. doi:10.1016/j.actamat.2016.05.047

Heczko, O., Lanska, N., Soderberg, O., Ullakko, K., 2002. Temperature variation of structure and magnetic properties of Ni-Mn-Ga magnetic shape memory alloys. J. Magn. Magn. Mater. 242–245, 1446–1449. doi:10.1016/S0304-8853(01)01087-3

Heczko, O., Seiner, H., Stoklasová, P., Sedlák, P., Sermeus, J., Glorieux, C., Backen, A., Fähler, S., Landa, M., 2018. Temperature dependence of elastic properties in austenite and martensite of Ni-Mn-Ga epitaxial films. Acta Mater. 145, 298–305. doi:10.1016/j.actamat.2017.12.011

Heczko, O., Sozinov, A., Ullakko, K., 2000. Giant field-induced reversible strain in magnetic shape memory NiMnGa alloy. IEEE Trans. Magn. 36, 3266–3268. doi:10.1109/20.908764

Heczko, O., Straka, L., 2003. Temperature dependence and temperature limits of magnetic shape memory effect. J. Appl. Phys. 94, 7139–7143. doi:10.1063/1.1626800

Heczko, O., Straka, L., Seiner, H., 2013. Different microstructures of mobile twin boundaries in 10 M modulated Ni-Mn-Ga martensite. Acta Mater. 61, 622–631. doi:10.1016/j.actamat.2012.10.007

Henry, C.P., 2002. Dynamic Actuation Properties of Ni-Mn-Ga Ferromagnetic Shape Memory Alloys. PhD thesis, Massachusetts Institute of Technology, USA.

Henry, C.P., Bono, D., Feuchtwanger, J., Allen, S.M., O'Handley, R.C., 2002. ac field-induced actuation of single crystal Ni–Mn–Ga. J. Appl. Phys. 91, 7810. doi:10.1063/1.1449441

Hobza, A., Patrick, C.L., Ullakko, K., Rafla, N., Lindquist, P., Müllner, P., 2018. Sensing strain with Ni-Mn-Ga. Sensors Actuators A Phys. 269, 137–144. doi:10.1016/j.sna.2017.11.002

Iadicola, M.A., Shaw, J.A., 2004. Rate and thermal sensitivities of unstable transformation behavior in a shape memory alloy. Int. J. Plast. 20, 577–605. doi:10.1016/S0749-6419(03)00040-8

Kainuma, R., Imano, Y., Ito, W., Sutou, Y., Morito, H., Okamoto, S., Kitakami, O., Oikawa, K., Fujita, A., Kanomata, T., Ishida, K., 2006. Magnetic-field-induced shape recovery by reverse phase transformation. Nature 439, 957–960. doi:10.1038/nature04493

Karaca, H., Karaman, I., Basaran, B., Chumlyakov, Y., Maier, H., 2006. Magnetic field and stress induced martensite reorientation in NiMnGa ferromagnetic shape memory alloy single crystals. Acta Mater. 54, 233–245. doi:10.1016/j.actamat.2005.09.004

Karaca, H.E., Karaman, I., Basaran, B., Ren, Y., Chumlyakov, Y.I., Maier, H.J., 2009. Magnetic field-induced phase transformation in NiMnColn magnetic shape-memory alloys-a new actuation mechanism with large work output. Adv. Funct. Mater. 19, 983–998. doi:10.1002/adfm.200801322

Kiefer, B., Lagoudas, D.C., 2005. Modeling of the magnetic field-induced martensitic variant reorientation and the associated magnetic shape memory effect in MSMAs. Proc. SPIE - Int. Soc. Opt. Eng. 5761, 454–465. doi:10.1117/12.600032

Kiefer, B., Lagoudas, D.C., 2004. Phenomenological modeling of ferromagnetic shape memory alloys.

SPIE, Smart Struct. Mater. 1, 14–18.

Lai, Y.W., 2009. Magnetic Microstructure and Actuation Dynamics of NiMnGa Magnetic Shape Memory Materials. PhD thesis, Technische Universität Dresden, Germany.

Lai, Y.W., Schafer, R., Schultz, L., McCord, J., 2008. Direct observation of AC field-induced twin-boundary dynamics in bulk NiMnGa. Acta Mater. 56, 5130–5137. doi:10.1016/j.actamat.2008.06.030

Liu, Y., Karaman, I., Wang, H., Zhang, X., 2014. Two types of martensitic phase transformations in magnetic shape memory alloys by in-situ nanoindentation studies. Adv. Mater. 26, 3893–8. doi:10.1002/adma.201400217

Liu, Y., Xie, Z.L., 2003. Twinning and detwinning of <0 1 1> type II twin in shape memory alloy. Acta Mater. 51, 5529–5543. doi:10.1016/S1359-6454(03)00417-8

Majewska, K.M., Żak, A.J., Ostachowicz, W.M., 2010. Vibration control of a rotor by magnetic shape memory actuators—an experimental work. Smart Mater. Struct. 19, 85004. doi:10.1088/0964-1726/19/8/085004

Molnar, P., Sittner, P., Lukas, P., Hannula, S.-P., Heczko, O., 2008. Stress-induced martensite variant reorientation in magnetic shape memory Ni–Mn–Ga single crystal studied by neutron diffraction. Smart Mater. Struct. 17, 35014. doi:10.1088/0964-1726/17/3/035014

Murray, S.J., Marioni, M., Allen, S.M., O'Handley, R.C., Lograsso, T.A., 2000. 6% magnetic-field-induced strain by twin-boundary motion in ferromagnetic Ni–Mn–Ga. Appl. Phys. Lett. 77, 886–888. doi:10.1063/1.1306635

O'Handley, R.C., Murray, S.J., Marioni, M., Nembach, H., Allen, S.M., 2000. Phenomenology of giant magnetic-field-induced strain in ferromagnetic shape-memory materials (invited). J. Appl. Phys. 87, 4712–4717. doi:10.1063/1.373136

Okamoto, N., Fukuda, T., Kakeshita, T., 2008. Temperature dependence of rearrangement of martensite variants by magnetic field in 10M, 14M and 2M martensites of Ni-Mn-Ga alloys. Mater. Sci. Eng. A 481–482, 306–309. doi:10.1016/j.msea.2006.12.218

Otsuka, K., C. M. Wayman, 1998. Shape Memory Materials. University of Illinois, Urbana-Champaign.

Pagounis, E., Chulist, R., Szczerba, M.J., Laufenberg, M., 2014. Over 7% magnetic field-induced strain in a Ni-Mn-Ga five-layered martensite. Appl. Phys. Lett. 105. doi:10.1063/1.4892633

Pascan, O.-Z., 2015. Dynamic behaviors of Ferromagnetic Shape Memory Alloys. PhD thesis, ENSTA-ParisTech, France.

Pascan, O.-Z., He, Y.J., Moumni, Z., Zhang, W.H., 2015. Temperature rise of high-frequency martensite reorientation via Type II twin boundary motion in NiMnGa Ferromagnetic Shape Memory Alloy. Scr. Mater. 104, 71–74. doi:10.1016/j.scriptamat.2015.04.006

Pascan, O., He, Y., Moumni, Z., Zhang, W., 2016. High-frequency performance of Ferromagnetic Shape Memory Alloys. Ann. Solid Struct. Mech. 8, 17–25.

Qu, Y.H., Cong, D.Y., Sun, X.M., Nie, Z.H., Gui, W.Y., Li, R.G., Ren, Y., Wang, Y.D., 2017. Giant and reversible room-temperature magnetocaloric effect in Ti-doped Ni-Co-Mn-Sn magnetic shape memory alloys. Acta Mater. 134, 236–248. doi:10.1016/j.actamat.2017.06.010

Rogovoy, A., Stolbova, O., 2016. Modeling the magnetic field control of phase transition in ferromagnetic shape memory alloys. Int. J. Plast. 85, 130–155. doi:10.1016/j.ijplas.2016.07.006

Sarawate, N., Dapino, M., 2008. Frequency Dependent Strain-Field Hysteresis Model for Ferromagnetic Shape Memory Ni-Mn-Ga. IEEE Trans. Magn. 44, 566–575. doi:10.1109/TMAG.2008.918316

Sarawate, N., Dapino, M., 2006. Experimental characterization of the sensor effect in ferromagnetic shape memory Ni-Mn-Ga. Appl. Phys. Lett. 88, 1–4. doi:10.1063/1.2189452

Saren, A., Musiienko, D., Smith, A.R., Tellinen, J., Ullakko, K., 2015. Modeling and design of a vibration energy harvester using the magnetic shape memory effect. Smart Mater. Struct. 24, 95002. doi:10.1088/0964-1726/24/9/095002

Sayyaadi, H., Amin, M., Farsangi, A., n.d. Frequency-dependent energy harvesting via magnetic shape memory alloys. Smart Mater. Struct. 24, 115022. doi:10.1088/0964-1726/24/11/115022

Sehitoglu, H., Wang, J., Maier, H.J., 2012. Transformation and slip behavior of Ni_2FeGa. Int. J. Plast. 39, 61–74. doi:10.1016/j.ijplas.2012.05.011

Shaw, J.A., Kyriakides, S., 1995. Thermomechanical aspects of NiTi. J. Mech. Phys. Solids 43, 1243–1281. doi:10.1016/0022-5096(95)00024-D

Smith, A.R., Tellinen, J., Ullakko, K., 2014. Rapid actuation and response of Ni-Mn-Ga to magnetic-field-induced stress. Acta Mater. 80, 373–379. doi:10.1016/j.actamat.2014.06.054

Soroka, A., Sozinov, A., Lanska, N., Rameš, M., Straka, L., Ullakko, K., 2018. Composition and temperature dependence of twinning stress in non-modulated martensite of Ni-Mn-Ga-Co-Cu magnetic shape memory alloys. Scr. Mater. 144, 52–55. doi:10.1016/j.scriptamat.2017.09.046

Sozinov, A., Lanska, N., Soroka, A., Straka, L., 2011. Highly mobile type II twin boundary in Ni-Mn-Ga five-layered martensite. Appl. Phys. Lett. 99, 124103. doi:10.1063/1.3640489

Sozinov, A., Soroka, A., Lanska, N., Rameš, M., Straka, L., Ullakko, K., 2017. Temperature dependence of twinning and magnetic stresses in $Ni_{46}Mn_{24}Ga_{22}Co_4Cu_4$ alloy with giant 12% magnetic field-induced strain. Scr. Mater. 131, 33–36. doi:10.1016/j.scriptamat.2016.12.032

Stephan, J.M., Pagounis, E., Laufenberg, M., Paul, O., Ruther, P., 2011. A Novel Concept for Strain Sensing Based on the Ferromagnetic Shape Memory Alloy NiMnGa 11, 2683–2689.

Straka, L., Drahokoupil, J., Pacherová, O., Fabiánová, K., Kopecký, V., Seiner, H., Hänninen, H., Heczko, O., 2016. The relation between lattice parameters and very low twinning stress in $Ni_{50}Mn_{25+x}Ga_{25-x}$ magnetic shape memory alloys. Smart Mater. Struct. 25, 25001. doi:10.1088/0964-1726/25/2/025001

Straka, L., Hänninen, H., Heczko, O., 2011a. Temperature dependence of single twin boundary motion in Ni-Mn-Ga martensite. Appl. Phys. Lett. 98. doi:10.1063/1.3573860

Straka, L., Heczko, O., Hannula, S.P., 2006. Temperature dependence of reversible field-induced strain in Ni-Mn-Ga single crystal. Scr. Mater. 54, 1497–1500. doi:10.1016/j.scriptamat.2005.12.046

Straka, L., Heczko, O., Seiner, H., Lanska, N., Drahokoupil, J., Soroka, A., Fähler, S., Hänninen, H., Sozinov, A., 2011b. Highly mobile twinned interface in 10M modulated Ni–Mn–Ga martensite: Analysis beyond the tetragonal approximation of lattice. Acta Mater. 59, 7450–7463. doi:10.1016/j.actamat.2011.09.020

Straka, L., Soroka, A., Seiner, H., Hänninen, H., Sozinov, A., 2012. Temperature dependence of twinning stress of Type I and Type II twins in 10M modulated Ni-Mn-Ga martensite. Scr. Mater. 67, 25–28. doi:10.1016/j.scriptamat.2012.03.012

Sutou, Y., Imano, Y., Koeda, N., Omori, T., Kainuma, R., Ishida, K., Oikawa, K., 2004. Magnetic and martensitic transformations of NiMnX(X=In, Sn, Sb) ferromagnetic shape memory alloys. Appl. Phys. Lett. 85, 4358–4360. doi:10.1063/1.1808879

Tan, H., Elahinia, M.H., 2008. A nonlinear model for ferromagnetic shape memory alloy actuators. Commun. Nonlinear Sci. Numer. Simul. 13, 1917–1928. doi:10.1016/j.cnsns.2007.03.019

Techapiesancharoenkij, R., Kostamo, J., Allen, S.M., C., R.O., 2011. The effect of magnetic stress and stiffness modulus on resonant characteristics of Ni–Mn–Ga ferromagnetic shape memory alloy actuators. J. Magn. Magn. Mater. 323, 3109–3116. doi:10.1016/j.jmmm.2011.06.066

Techapiesancharoenkij, R., Kostamo, J., Allen, S.M., O'Handley, R.C., 2009. Frequency response of acoustic-assisted Ni–Mn–Ga ferromagnetic-shape-memory-alloy actuator. J. Appl. Phys. 105, 93923. doi:10.1063/1.3125307

Vronka, M., Seiner, H., Heczko, O., 2017. Temperature dependence of twinning stress – Analogy between Cu–Ni–Al and Ni–Mn–Ga shape memory single crystals. Philos. Mag. 97, 1479–1497. doi:10.1080/14786435.2017.1303577

Xia, M., Sun, Q., 2017. Thermomechanical responses of nonlinear torsional vibration with NiTi shape memory alloy – Alternative stable states and their jumps. J. Mech. Phys. Solids 102, 257–276. doi:10.1016/j.jmps.2016.11.015

Xia, M., Sun, Q., 2015. Jump phenomena of rotational angle and temperature of NiTi wire in nonlinear torsional vibration. Int. J. Solids Struct. 56, 220–234. doi:10.1016/j.ijsolstr.2014.11.002

Yin, R., Wendler, F., Krevet, B., Kohl, M., 2016. A magnetic shape memory microactuator with intrinsic position sensing. Sensors Actuators, A Phys. 246, 48–57. doi:10.1016/j.sna.2016.05.013

Yu, C., Kang, G., Song, D., Kan, Q., 2015. Effect of martensite reorientation and reorientation-induced plasticity on multiaxial transformation ratchetting of super-elastic NiTi shape memory alloy: New consideration in constitutive model. Int. J. Plast. 67, 69–101. doi:10.1016/j.ijplas.2014.10.001

Zhao, D., Liu, J., Chen, X., Sun, W., Li, Y., Zhang, M., Shao, Y., Zhang, H., Yan, A., 2017. Giant caloric effect of low-hysteresis metamagnetic shape memory alloys with exceptional cyclic functionality. Acta Mater. 133, 217–223. doi:10.1016/j.actamat.2017.05.020

Zou, N., Li, Z., Zhang, Y., Yang, B., Zhao, X., Esling, C., Zuo, L., 2017. Plastic deformation of Ni-Mn-Ga 7M modulated martensite by twinning & detwinning and intermartensitic transformation. Int. J. Plast. 100, 1–13. doi:10.1016/j.ijplas.2017.07.006

Zreihan, N., Faran, E., Shilo, D., 2016. The effects of temperature on the lattice barrier for twin wall motion. Appl. Phys. Lett. 41605. doi:10.1063/1.4927660

- Energy dissipation during high-frequency martensite reorientation can cause significant temperature rise, which might result in phase transformation and make the dynamic output strain of FSMA at risk of instability (strain reduction).
- The stable strain amplitude and the stable temperature of FSMA can be controlled by the ambient heat-exchange efficiency.
- The stable strain amplitude depends on the heat-exchange efficiency non-monotonically.
- An “isothermal” FSMA-actuator with tunable output strain is proposed based on the coupling of temperature-induced phase transformation and magnetic-field-induced martensite reorientation.